1. Extended Data

Figure #	Figure title One sentence only	Filename This should be the name the file is saved as when it is uploaded to our system. Please include the file extension. i.e.: *Smith_ED_Fi_1.jpg*	Figure Legend If you are citing a reference for the first time in these legends, please include all new references in the Online Methods References section, and carry on the numbering from the main References section of the paper.
Extended Data Fig. 1	**Polar skyrmion structure in $[(SrTiO_3)_{16}/(PbTiO_3)_{16}]_8$ superlattice.**	Extended_Data_Fig 1	**Polar skyrmion structure in $[(SrTiO_3)_{16}/(PbTiO_3)_{16}]_8$ superlattice. a,** Planar-view dark-field STEM imaging shows the widespread occurrence of nanometer-size (~8 nm) skyrmion formation along the [100] and [010] directions. **b,** Second-principles calculations of the skyrmion structure in the superlattice. The hedgehog-like skyrmion (Topological number +1) at the top and bottom interface between $SrTiO_3$ and $PbTiO_3$, and the Bloch-like skyrmion (topological number +1) at the central plane in $PbTiO_3$ are clearly visible. The arrows represent the normalized electric dipole moments.
Extended Data Fig. 2	**Synchrotron-based symmetric three-dimensional reciprocal space mapping about the (002) diffraction condition of the $SrTiO_3$ substrate**.	Extended_Data_Fig 2	**Synchrotron-based symmetric three-dimensional reciprocal space mapping about the (002) diffraction condition of the $SrTiO_3$ substrate**. Reciprocal space mapping of **a,** $(SrTiO_3)_{16}$ /$(PbTiO_3)_{16}$/$(SrTiO_3)_{16}$ trilayer, **b,** $[(PbTiO_3)_{16}/(SrTiO_3)_{16}]_3$ superlattice, **c,** $[(PbTiO_3)_{16}/(SrTiO_3)_{16}]_5$ superlattice and **d,** $[(PbTiO_3)_{16}/(SrTiO_3)_{16}]_8$ superlattice. The satellite peaks along (100) direction (side-lobes; white arrow) which correspond to the skyrmions.
Extended Data Fig. 3	**Loss Tangent as a function of electric field.**	Extended_Data_Fig 3	**Loss Tangent as a function of electric field.** The loss tangent (tanδ) as a function of electric field for **a,** $[(SrTiO_3)_{16}/(PbTiO_3)_{16}]_8$ superlattice, **b,** $[(SrTiO_3)_{16}/(PbTiO_3)_{16}]_5$ superlattice, **c,** $[(SrTiO_3)_{16}/(PbTiO_3)_{16}]_3$ superlattice, **d,**

			$(SrTiO_3)_{16}/(PbTiO_3)_{16}/(SrTiO_3)_{16}$ trilayer which is in the skyrmion state compared to its constituents **e,** 50nm $SrTiO_3$ (brown) and **f,** 50 nm-thick $PbTiO_3$ layer.
Extended Data Fig. 4	**Measured out-of-plane dielectric permittivity as a function of electric field for the**	Extended_Data_Fig 4	**Measured out-of-plane dielectric permittivity as a function of electric field for the a,** $[(SrTiO_3)_{16}/(PbTiO_3)_{16}]_8$ superlattice (skyrmion sample) compared with 50nm $SrTiO_3$ and 50 nm $PbTiO_3$ layers on $SrTiO_3$ (001) and **b,** $[(SrTiO_3)_{16}/(PbTiO_3)_{16}]_8$ superlattice (vortex sample) compared with 50nm $SrTiO_3$ and 50 nm $PbTiO_3$ layers on $DyScO_3$ (110) substrate. The enhancement of dielectric permittivity for the skyrmion sample ~ 20X larger compared to its series permittivity whereas it only ~ 9X for vortex samples.
Extended Data Fig. 5	**Out-of-plane dielectric permittivity as a function of frequency measured on three different devices.**	Extended_Data_Fig 5	**Out-of-plane dielectric permittivity as a function of frequency measured on three different devices. a,** Capacitance vs Frequency of $[(SrTiO_3)_{16}/(PbTiO_3)_{16}]_8$ superlattice (superlattice total thickness: 100nm, capacitor size of the measurement: 25μm) compared with 50nm $PbTiO_3$ (orange), 50nm $SrTiO_3$ layers (brown) (capacitor size of the measurement: 25 μm) at electric field E=0 kV/cm and E=1000 kV/cm (light green). **b,** Tangent loss ($\tan\delta$) vs Frequency of $[(SrTiO_3)_{16}/(PbTiO_3)_{16}]_8$ superlattice compared with 50nm $PbTiO_3$ (orange) and 50nm $SrTiO_3$ (brown) layers. It shows the Tanδ which is approximately an order of magnitude smaller than for samples which show Maxwell-Wagner (MW) effects in the literature (Ref. 24, 25). **c,** Dielectric permittivity vs Frequency of $[(SrTiO_3)_{16}/(PbTiO_3)_{16}]_8$ superlattice which is in the skyrmion state measured in three different capacitor devices compared with 50nm $PbTiO_3$ (orange) and 50nm $SrTiO_3$ (brown) layers at electric field E=0 kV/cm and E=1000 kV/cm (light green). **d,**

			Capacitance (left axis), permittivity (right axis) as a function of electric field of $[(SrTiO_3)_{16}/(PbTiO_3)_{16}]_8$ superlattice which is in the skyrmion state at 10kHz (blue), 100kHz (red) and 1MHz (green). The capacitance and permittivity change by ~ 4% over the measured frequency range. This reveals that the calculated negative permittivity from this macroscopic measurement is independent of measured frequency in this range. 24 D. O'Neill, D., Bowman, R.M and Gregg, J.M. Dielectric enhancement and Maxwell–Wagner effects in ferroelectric superlattice structures. *Appl. Phys. Lett.* **77**, 1520-1522 (2000). 25 Catalan, G., D. O'Neill, D., Bowman, R.M and Gregg. J.M. Relaxor features in ferroelectric superlattices: A Maxwell–Wagner approach. *Appl. Phys. Lett.* **77**, 3078-3080 (2000).
Extended Data Fig. 6	**In-plane dielectric permittivity of $[(SrTiO_3)_{16}/(PbTiO_3)_{16}]_8$ superlattice at microwave frequencies from 100**	Extended_Data_Fig 6	**In-plane dielectric permittivity of $[(SrTiO_3)_{16}/(PbTiO_3)_{16}]_8$ superlattice at microwave frequencies from 100 MHz to 10 GHz. a,** A schematic of co-planar Waveguide (CPW) transmission lines for microwave-frequency permittivity characterization. **b,** A cross-sectional view of the CPW illustrating the electric

	MHz to 10 GHz.		fields between the center conductor and ground planes. **c,** A circuit model of the CPW transmission line showing how the total measured capacitance of the transmission line (C) is comprised of a portion related to the permittivity of the $SrTiO_3$ substrate (C_{SUB}), and a portion related to the permittivity of the superlattice (C_{FILM}). **d,** The measured capacitance of the CPW transmission lines on the superlattice (purple), and $SrTiO_3$ substrate (red) are shown. Finite element simulations and the measurements of the bare $SrTiO_3$ substrate are used to analyze and isolate the portion of the total capacitance which is related to the permittivity of the superlattice (blue). **e,** The real part of the in-plane dielectric permittivity (left-hand y-axis) and the loss tangent (right-hand y-axis) are determined from the capacitance and conductance measurements via a mapping function obtained from 2D finite element modeling of the CPW structures; **f,** Cole-Cole model of the in-plane complex permittivity of the superlattice from 100 MHz to 10 GHz (Supplementary Note 2).
Extended Data Fig. 7	**Phase field simulation of the switching dynamics of skyrmions under different externally applied fields**.	Extended_Data_Fig 7	**Phase field simulation of the switching dynamics of skyrmions under different externally applied fields**. The size of the skyrmion decreases progressively until all the skyrmions implode at ~1500 kV/cm. **a,** positive field. **b,** negative field.
Extended Data Fig. 8	**Second principle simulation of the evolution of the local polarization texture at the central layer of the $PbTiO_3$ under different external**	Extended_Data_Fig 8	**Second principle simulation of the evolution of the local polarization texture at the central layer of the $PbTiO_3$ under different external fields.** The arrows represent the polarization on the x-y plane, while the colors represent the component of the out-of-plane polarization as indicated in the legend. The snapshots correspond to Monte Carlo simulations at different

	fields.		electric fields, where the initial configuration for a new magnitude of the field was the relaxed structure from the previous field. **a,** positive field. **b,** negative field. For the sake of clarity let us assume that the core of the skyrmion has a polarization pointing along the +*z* direction, while it points down along -*z* at the periphery, at null external field. Let us assume also that we switch on an external field parallel to the polarization at the center of the skyrmion, as it is done in panel (a) (positive values of the field). Then, as it is clearly visible from the snapshots at 250 kV/cm and 500 kV/cm, the domain with a polarization parallel to the external field increases at the expenses of the other. The domain wall of the skyrmion has moved, but there will be always a domain wall between the core and the periphery of the skyrmion where the out-of-plane polarization vanishes (see the regions plotted in white delimiting the surface of the skyrmion). There is a tendency of the domain wall to polarize with the appearance of a Bloch component to minimize the energy (see the arrows within the white regions of the panels).[48] This Bloch components of the polarization are perpendicular to the applied field and do not couple with it. Therefore, they will be always present, independently of the sizes of the domains up and down. These Bloch components closing a loop around the domain wall are precisely at the origin of the non-trivial topological textures (the vortex they form determine why the skyrmion number is +1). The larger the electric field, the larger the size of the domain that aligns with it (with the criterion chosen for this example, the skyrmion expands). For a critical field, this domain will cover all space and the transition to a monodomain state will be completed. Right before the

			transition, a singularity appears: the stereographic projection of our dipole patterns does not completely wrap the unit sphere. That is exactly the point where the skyrmion number changes from +1 (non-trivial topological structure) to 0 (trivial case in the monodomain configuration). [48]Wojdeł, J.C. and Íñiguez, J., Ferroelectric transitions at ferroelectric domain walls found from first-principles. *Phys. Rev. Lett.* **112**, 247603 (2014).
Extended Data Fig. 9	**Tunable skyrmion size under electric field as a basis for dielectric enhancement $[(SrTiO_3)_{16}/(PbTiO_3)_{16}]_8$ superlattice.**	Extended_Data_Fig 9	**Tunable skyrmion size under electric field as a basis for dielectric enhancement $[(SrTiO_3)_{16}/(PbTiO_3)_{16}]_8$ superlattice. a,** Experimental line cuts through skyrmion diffuse scattering showing 1st and 2nd order satellites, including their suppression and enhancement, respectively, under external electric field. **b,** Electric field dependency of 1st and 2nd order satellites shown in **a,** determined experimentally. **c,** Phase field model of vertical polarization distribution versus electric field depicting planar cuts (80 nm × 80 nm) through the center and parallel with the $PbTiO_3$ layer. Insets show FFT averages for all $PbTiO_3$ layers of the superlattice, which indicates the emergence of 2nd order diffuse scattering skyrmion ring in addition to the dominant 1st order diffuse scattering skyrmion ring. The 2nd order ring intensity is enhanced under application of electric field relative to without field. **d,** Comparison between the experimentally estimated and phase-field calculated skyrmion areal fraction inside $PbTiO_3$ layers of the superlattice. **g,** Comparison between the experimentally measured (blue) and phase- field calculated (red) dielectric permittivity of the superlattice, which is closely mapped with electric

			field dependent normalized satellite intensity of skyrmion calculated from reciprocal space (dark gray, right axis).
Extended Data Fig. 10	**Temperature control of skyrmion of $[(SrTiO_3)_{16}/(PbTiO_3)_{16}]_8$ superlattice.**	Extended_Data_Fig 10	**Temperature control of skyrmion** of **$[(SrTiO_3)_{16}/(PbTiO_3)_{16}]_8$ superlattice. a-c,** Temperature dependent three-dimensional, synchrotron-based symmetric reciprocal space mapping about the (002) diffraction condition of the $SrTiO_3$ substrate. The satellite peaks along (100) direction (side-lobes) which correspond to the skyrmions. **d,** The in-plane satellite peaks intensity (skyrmion peaks) diminishing upon heating and completely disappeared ~600K. **e,** Comparison between the temperature-dependent experimentally measured and phase- field calculated out-of-plane dielectric permittivity of the superlattice.

Delete rows as needed to accommodate the number of figures (10 is the maximum allowed).

2. Supplementary Information:

A. Flat Files

Item	Present?	Filename This should be the name the file is saved as when it is uploaded to our system, and should include the file extension. The extension must be .pdf	A brief, numerical description of file contents. i.e.: *Supplementary Figures 1-4, Supplementary Discussion, and Supplementary Tables 1-4.*
Supplementary Information	Yes	Supplementary_Information_Negative_Capacitance_Polar Skyrmion	Supplementary Note 1-4 Supplementary Figs. 1-10 Supplementary Tables 1-2 Supplementary References 1-7.
Reporting Summary	No		

B. Additional Supplementary Files

Type	Number If there are multiple files of the same type this should be the numerical indicator. i.e. "1" for Video 1, "2" for Video 2, etc.	Filename This should be the name the file is saved as when it is uploaded to our system, and should include the file extension. i.e.: *Smith_ Supplementary_Video_1.mov*	Legend or Descriptive Caption Describe the contents of the file
Choose an item.			

3. Source Data

Parent Figure or Table	Filename This should be the name the file is saved as when it is uploaded to our system, and should include the file extension. i.e.: *Smith_SourceData_Fig1.xls,* or *Smith_ Unmodified_Gels_Fig1.pdf*	Data description e.g.: Unprocessed Western Blots and/or gels, Statistical Source Data, etc.
Source Data Fig. 1		

Local negative permittivity and topological-phase transition in polar skyrmions

S. Das[1,2*#], Z. Hong[3,4*], V.A. Stoica[3*], M. A. P. Gonçalves[5,6,7*], Y.T. Shao[8], E. Parsonnet[2], E. J. Marksz[9], S. Saremi[1], M. R. McCarter[2], A. Reynoso[2], C. J. Long[9], A. M. Hagerstrom[9], D. Meyers[1], V. Ravi[1], B. Prasad,[1] H. Zhou[10], Z. Zhang[10], H. Wen[10], F. Gómez-Ortiz[6], P. García-Fernández[6], J. Bokor[11], J. Íñiguez[5,7], J.W. Freeland[10], N. D. Orloff[9], J. Junquera[6], L.Q. Chen[3], S. Salahuddin[11], D. A. Muller[8,12], L.W. Martin[1,13], R. Ramesh[1,2,13#]

[1] Department of Materials Science and Engineering, University of California, Berkeley, California 94720, USA

[2] Department of Physics, University of California, Berkeley, California 94720, USA

[3] Department of Materials Science and Engineering, The Pennsylvania State University, University Park, Pennsylvania 16802, USA

[4] Department of Mechanical Engineering, Carnegie Mellon University, Pittsburgh, PA 15213, USA.

[5] Materials Research and Technology Department, Luxembourg Institute of Science and Technology (LIST), 5 avenue des Hauts-Fourneaux, L-4362 Esch/Alzette, Luxemburg

[6] Departamento de Ciencias de la Tierra y Física de la Materia Condensada, Universidad de Cantabria, Cantabria Campus Internacional, Avenida de los Castros s/n, E-39005 Santander, Spain

[7] Physics and Materials Science Research Unit, University of Luxembourg, 41 Rue du Brill, L-4422 Belvaux, Luxembourg

[8] School of Applied and Engineering Physics, Cornell University, Ithaca, NY, USA

[9] National Institute of Standards and Technology, Boulder, CO, USA

[10] Advanced Photon Source, Argonne National Laboratory, Argonne, IL, USA

[11] Department of Electrical Engineering and Computer Sciences, University of California, Berkeley, CA, USA

[12] Kavli Institute at Cornell for Nanoscale Science, Ithaca, New York 14853, USA

[13] Materials Sciences Division, Lawrence Berkeley National Laboratory, Berkeley, California 94720, USA

(* these authors contributed equally)

The author to whom correspondence: S.D (sujitdas@berkeley.edu) or R.R. (rramesh@berkeley.edu)

Topological solitons such as magnetic skyrmions have drawn attention as stable quasi-particle-like objects. The recent discovery of polar vortices and skyrmions in ferroelectric-oxide superlattices has opened up new vistas to explore topology, emergent phenomena, and approaches for manipulating such features with electric fields. Using macroscopic dielectric measurements, coupled with direct scanning convergent-beam electron diffraction (SCBED) imaging at the atomic scale, theoretical phase-field simulations, and second-principles calculations, we demonstrate that polar skyrmions in $(PbTiO_3)_n/(SrTiO_3)_n$ superlattices are distinguished by a sheath of negative permittivity at the periphery of each skyrmion. This enhances the effective dielectric permittivity compared to individual $SrTiO_3$ and $PbTiO_3$ layers. Moreover, the response of these topologically protected structures to electric field and temperature show a reversible phase transition from the skyrmion state to a trivial uniform ferroelectric state, accompanied by large tunability of the dielectric permittivity. Pulsed-switching measurements show a time-dependent evolution and recovery of the skyrmion state (and macroscopic dielectric response). The interrelationship between topological and dielectric properties presents an opportunity to simultaneously manipulate both of them by a single, and easily controlled, stimulus, the applied electric field.

Spatially complex, real-space topological configurations and their phase transitions have recently emerged as a fertile playground in condensed-matter physics.[1,2,3,4] Although the focus has been on spin textures in magnets,[4,5,6] leading to the formation of skyrmions and related topologically protected states, in recent years there has been renewed efforts to discover analogous charge textures in, for example, ferroelectrics.[7-10] With the discovery of such polar textures (*e.g.*, vortices and skyrmions), it is of both fundamental and practical interest to understand the microscopic and macroscopic nature of their dielectric response and the possibility of a field-driven topological-phase transition.[1,2]

In parallel, the possibility of capturing "negative permittivity" states in ferroelectrics, either in the temporal (*i.e.*, dynamical) or spatial (*i.e.*, in equilibrium) domain has drawn the attention of scientists and engineers alike.[11,12,13,14,15,16,17,18,19] The concept of negative capacitance was developed in monodomain ferroelectric capacitors by considering that upon transitioning to a ferroelectric state, a material develops a classic "double-well potential energy" landscape. The minima of these wells represent the equilibrium state of the material and the curvature of the energy landscape dictates that small electric-field perturbations should give rise to classical positive capacitive response (*i.e.*, positive permittivity). It was proposed, however, that if one could place the material in the region between these two states (*i.e.*, in a region of negative curvature of the energy landscape) it could give rise to a negative-capacitive response (*i.e.*, negative permittivity) under electric-field excitation.[2,20] In a capacitor heterostructure comprised of an ideal ferroelectric capacitor (capacitance C_F) in series with a regular dielectric capacitor (capacitance C_D), the overall capacitance $C = (C_F^{-1} + C_D^{-1})^{-1}$ has to be positive for thermodynamic stability. But if $C_F < 0$, the total C will be larger than any of the two constituent capacitors taken independently. Accessing this regime, however, remains a challenge in the static

sense[14,16,18]: if the capacitor is driven by a voltage the region of negative curvature is unstable. Researchers have explored approaches wherein the capacitor is driven by a charge, that can be simply controlled in an electrostatically coupled ferroelectric/dielectric series capacitor.[13] If it is a dielectrically stiff material, it will effectively suppress the spontaneous polarization of the ferroelectric and thus to stabilize the paraelectric state even if the ferroelectric is below its nominal transition temperature.[18] The negative-capacitance effect was first proposed in ferroelectric bilayers[11] as well as in several ferroelectrics as transient states.[21,22] Recent work has further demonstrated that in multidomain ferroelectric polar structures – such as the vortices found in $(PbTiO_3)_n/(SrTiO_3)_n$ superlattices – the complex polar order, while producing an overall positive dielectric permittivity, exhibits regions of varying dielectric susceptibility including areas of local negative-capacitive response in the $PbTiO_3$ layers.[2]

The recent discovery of chiral polar skyrmions in $(PbTiO_3)_n/(SrTiO_3)_n$ superlattices by the interplay of elastic, electrostatic, and gradient energies with a topological number of +1 raises a fundamentally important question: do such skyrmions also exhibit a spatial distribution of varying dielectric susceptibility?[1] Here, we demonstrate a strong enhancement of the out-of-plane dielectric permittivity and that this is a direct consequence of a negative-permittivity region that forms at the periphery of each skyrmion. In this region, the polarization is more susceptible to external stimuli than the inner core or the outer regions of the skyrmions. This is further confirmed by second-principles calculations, phase-field modeling, and direct microscopic measurements of the local potential energy via scanning convergent-beam electron diffraction (SCBED) experiments using an electron microscopy pixel array detector (EMPAD). The macroscopic permittivity also exhibits a large electric-field tunable response which arises from the conversion of the skyrmions into a uniformly polarized state (topological-phase

transition), as evidenced by both electric-field- and temperature-dependent dielectric measurements and synchrotron-based-diffraction studies, which are supported by second-principles calculations and phase-field simulations.

Macroscopic details of negative capacitance in polar skyrmions

A series of $[(PbTiO_3)_{16}/(SrTiO_3)_{16}]_m$ superlattices (m = 3, 5, 8) and $(SrTiO_3)_{16}/(PbTiO_3)_{16}/(SrTiO_3)_{16}$ trilayers (where the subscript numbers refer to the number of unit cells) as well as 50 nm-thick $SrTiO_3$ and 50 nm-thick $PbTiO_3$ single-layer thin films all grown on TiO_2-terminated single-crystalline $SrTiO_3$ (001) substrates, with epitaxial $SrRuO_3$ top and bottom electrodes (all films produced via reflection high-energy electron diffraction (RHEED)-assisted pulsed-laser deposition; Methods) were synthesized for this study.[1] Plan-view scanning transmission electron microscopy (STEM) images of the superlattices reveal an array of skyrmion bubbles (8-9 nm in diameter) (Extended Data Fig. 1a), the formation of which has been confirmed by second-principles calculations (Extended Data Fig. 1b)[1] which reveal that they are indeed electric analogs of magnetic skyrmions and have a mathematically definable and characteristic skyrmion number of +1 (Supplementary Table 1). Three-dimensional reciprocal space mapping (RSM) studies of the superlattices about the 002-diffraction condition show satellite peaks around the film peak along the in-plane directions (side lobes), corresponding to an ordered phase (*i.e.*, the skyrmion phase) with a periodicity of 8-9 nm (Extended Data Fig. 2).[1] In all heterostructures studied – the superlattices, trilayers, and single-layer films – all layers were found to be coherently strained to the underlying $SrTiO_3$ substrate, confirming that the strain state in all cases is the same. Macroscopic measurements of the dielectric permittivity (extracted from the experimentally measured capacitance, Figure 1a) and dielectric loss (Extended Data Fig. 3) as a function of electric field (applied normal to the surface) for

$[(PbTiO_3)_{16}/(SrTiO_3)_{16}]_m$ superlattices (m = 3, 5, 8) and $(SrTiO_3)_{16}/(PbTiO_3)_{16}/(SrTiO_3)_{16}$ trilayers were completed. The superlattices and the trilayer exhibit a strong enhancement of zero-field dielectric permittivity compared to the various single-layer $SrTiO_3$ and $PbTiO_3$ heterostructures (Fig. 1a), contrary to what is expected to be a decrease in the overall permittivity as calculated using a conventional "dielectrics in series" scenario ("Series permittivity" dotted line, Fig. 1a and Extended Data Fig. 4). These structures also show large electric-field tunability (~70-80% for the various superlattices and trilayers under 1500 kV/cm fields); which is significantly different from that of the single-layer $SrTiO_3$ (~7% under 700 kV/cm) and $PbTiO_3$ (~2% under 700 kV/cm) (Fig. 1a) as well as the polar vortices [which form when the superlattice is synthesized on $DyScO_3$ (110)], which show the electric field tunability of almost 45% (Extended Data Fig. 4, Supplementary Table 2).[2]

Phase-field, second-principles simulations and theoretical rationalization

In order to understand the microscopic origins of the dielectric observations, we carried out detailed phase-field simulations and second-principles calculations for $[(PbTiO_3)_{16}/(SrTiO_3)_{16}]_8$ superlattices to extract measures of the dielectric permittivity (Methods and Supplementary Fig. 1). The normalized electric-field-dependent permittivity from both these theoretical approaches are captured [red dashed (phase-field) and green dashed (second-principles) lines, Fig. 1b] and closely follow the experimental data. The origin of such an enhancement in the dielectric permittivity can be unraveled from the theoretical simulations which provide spatially-resolved maps of the local permittivity (Fig. 2). Taking a real-space representation of the skyrmions (left, Fig. 2a), we can extract the corresponding spatial distribution of the dielectric permittivity within the $PbTiO_3$ layer from the phase-field simulations (right, Fig. 2a). This indicates an unusual

dielectric state within the $PbTiO_3$ layer wherein there are regions of negative permittivity (blue/cyan regions, Fig. 2a and Supplementary Fig. 2) at the wall of the skyrmion. Inside and outside this surface region, the permittivity is positive (yellow regions, Fig. 2a). The inverse of the dielectric permittivity from the second-principles calculations for a single skyrmion (Fig. 2b and Supplementary Fig. 3) also reveals the existence of a region of negative permittivity at the periphery of the skyrmions. The corresponding electric susceptibility (Fig. 2c and Supplementary Fig. 3) also reveals that the wall of the skyrmion exhibits the highest electric susceptibility and deforms with an applied electric field to increase/decrease the volume of the core.

Based on these calculations, it is possible to reconstruct the macroscopic dielectric permittivity of the $[(PbTiO_3)_{16}/(SrTiO_3)_{16}]_8$ superlattices (Supplementary Note 1 and schematically illustrated in Fig. 2d). While the superlattices consist of $SrTiO_3$ and $PbTiO_3$ layers connected in series, the $PbTiO_3$ layers have two regions, one inside/outside the skyrmions with positive permittivity and the other at the wall of the skyrmions with negative permittivity, which are electrically parallel to each other (Fig. 2d). Based on this structure, an "effective circuit" model for this stack (right, Fig. 2d) enables us to calculate the net permittivity of the superlattice as a function of the individual dielectric permittivities of the $SrTiO_3$ (ε_1), $PbTiO_3$ within/without the skyrmion (ε_2), and $PbTiO_3$ within the skyrmion boundary (ε_3) (Fig. 2e, f). There are a few key conclusions that emerge from these calculations: for normal values of the permittivity of $SrTiO_3$ and $PbTiO_3$ (i.e., values less than 300), the permittivity of the skyrmion wall (ε_3) is negative (Fig. 2e, f) in order to obtain an effective dielectric permittivity of the superlattice around 800, consistent with the results shown in Fig. 1a. Positive values of the skyrmion wall permittivity can be obtained for non-reasonable values of the permittivity of the $SrTiO_3$ and $PbTiO_3$ layers: for example, identified by the data points with fictitious permittivities (Fig.

2e). These scenarios seem unlikely since it would mean that simultaneously, both $SrTiO_3$ and the $PbTiO_3$ layer as a whole have a significantly enhanced permittivity compared to the bulk (Supplementary Note 1). Based on these calculations and the experimental measurements, we estimate the permittivity of the skyrmion wall to be ~ -900, which is qualitatively consistent with phase-field simulations and second-principles calculations (Fig. 2a-c). Comparisons of the dielectric permittivity of the vortex and the skyrmion (Extended Data Fig. 4) show that they are significantly different from each other. We note that although large enhancements in dielectric permittivity have been observed in other systems (relaxor ferroelectrics, functionally graded ferroelectrics, etc.) [23], the fundamental physical origins of the enhancement in the dielectric response in this case is completely different from other possible phenomena (*e.g.*, Maxwell-Wagner effects, inductor-capacitor (LC) resonance)[24,25,26], again suggesting that it is intimately associated with the skyrmion state. The measured out-of-plane capacitance (permittivity) (Extended Data Fig. 5) show a linear-logarithmic frequency dependence, decreasing by approximately 4% per decade across the measured range from 10^2 Hz to 10^6 Hz. Theoretical models on the electrodynamics of ferroelectric thin films with negative capacitance suggest that the strongest variations with respect the static limit should appear in the resonance THz regime, orders of magnitude larger than the ones explored in the present work.[27] This behavior is not present in measured capacitance and permittivity of the single-composition $PbTiO_3$ and $SrTiO_3$ films, and therefore likely indicates dynamic effects of the skyrmions at these frequencies (details of the frequency dependence of in-plane capacitance and permittivity are presented in Extended Data Fig. 6 and Supplementary Note 2[28,29]).

Microscopic observation of negative capacitance at skyrmion walls

The possibility of the existence of such a region of negative permittivity at the skyrmion wall and the potential-energy landscape across the skyrmion can be directly probed using scanning convergent beam electron diffraction (SCBED) experiments. These imaging experiments were carried out in cross-section samples so that we could image both the Neél and Bloch components edge-on (Fig. 3a).[1] The SCBED experiments were performed using an electron microscopy pixel array detector (EMPAD) (Supplementary Fig. 4 and Methods) which records the full momentum distribution (*i.e.*, the electron diffraction pattern) at every scan position, providing information to measure both the ferroelectric polarization and electric field simultaneously and independently (Fig. 3b-d). For this study, we focused on the deflection of the (000) beam since there are fewer polarity effects. The polarization direction is quantitatively determined from the diffraction intensity differences of Friedel pairs, such as the (100)/($\bar{1}$00) and (001)/(00$\bar{1}$) for the x and z component of polarity, respectively (Fig. 3b, Supplementary Fig. 4, and Methods).[2] The long-range electric fields can be reconstructed from the deflection of the entire CBED pattern due to the Lorentz force (Fig. 3c, Supplementary Fig. 4, and Methods).[2, 30] Focusing along the dashed horizontal line profile (Fig. 3b,c), which goes through the center of a skyrmion, we can extract information about the walls of the skyrmion (Fig. 3a)[1] by measuring the polarization (P_z) and electric field (E_z) along this line (Fig. 3d). The magnitude of the measured polarization was calibrated using the polarization of $PbTiO_3$ as reference.[31] With both the measured electric field and polarization, we can estimate the local potential energy of the system following the approach given in Ref. 2. The estimated potential-energy (G) as a function of P_z across the skyrmion (Fig. 3e; details in Methods) reveals the existence of a local potential-energy maxima ($\partial^2 G/\partial P^2 < 0$) at the location of the skyrmion wall, where P_z is small (Fig. 3e). This supports the existence of

regions having negative curvature of the free energy (*i.e.*, negative permittivity) in the skyrmion walls.

Field- and temperature-driven permittivity and topological phase transition

Having identified a possible source of the enhancement of overall permittivity associated with the negative permittivity at the skyrmion wall, we now discuss the changes in the dielectric response and the topological structure with electric field (Fig. 4). Both phase-field simulations and second-principles calculations reveal that when an electric field is applied along the out-of-plane direction (parallel/antiparallel to the uniform polarization of the skyrmion cores) it progressively expands (shrinks) for parallel (antiparallel) fields and ultimately the entire material becomes uniformly poled with increasing field (Fig. 4a-c and Extended Data Figs. 7, 8). To validate these calculations, we performed electric-field-dependent X-ray diffraction RSM studies (Methods) to observe the skyrmion evolution[1] as a function of applied electric field. The electric-field-dependent RSM studies (Fig. 4d-f and Supplementary Fig. 5) show the systematic disappearance of the skyrmion-satellite peaks with increasing electric field, indicating field-induced structural changes related to the skyrmions (Fig. 4e-f, Extended Data Figs. 9a-c and Supplementary Fig. 5, 6). The external electric field in the out-of-plane direction breaks the symmetry and tends to align the dipoles along the direction of the external field in order to minimize the energy.[32,33] The electric-field-driven change in the size of the skyrmion directly impacts the effective dielectric permittivity as well as the negative component of permittivity (Supplementary Note 3, Extended Data Fig. 9d and Supplementary Fig. 7). The calculated and the experimentally measured dielectric permittivity are in close quantitative agreement. Also, the normalized intensity of the skyrmion satellite peaks closely resembles the trends in the evolution

of the electric-field dependence of the permittivity (dark gray, Extended Data Fig. 9e). The same trend is observed in the temperature-dependent change of effective dielectric permittivity of the superlattice (Extended Data Fig. 10) which closely follows the experimentally measured temperature-dependent permittivity.

Such polar skyrmions are characterized mathematically by the topological charge/number, $N_{\mathrm{Q}} = \frac{1}{4\pi}\iint \vec{u}\cdot\left(\frac{\partial\vec{u}}{\partial x}\times\frac{\partial\vec{u}}{\partial y}\right) dxdy$, where $\vec{u}$ denotes the normalized local dipole moment, and the surface integral is taken over the corresponding (001) plane. The integrand is the Pontryagin density, and its surface integral is the topological number of the observed skyrmion, which takes an integer value of +1 as confirmed by phase-field and second-principles simulations.[1] Our simulations suggest a topological transition from a skyrmion state to uniform ferroelectric state at an electric field $\gtrsim$ 1500 kV/cm. Below this threshold, their Pontryagin density is finite (Supplementary Fig. 8) and the topological number remains +1 (Fig. 4g). Above this field, the skyrmion disappears indicating that the polarization texture is unstable and transforms to a uniform ferroelectric state with a trivial $N_{\mathrm{Q}} = 0$ (Fig. 4g, Extended Data Fig. 7,8 and Supplementary Fig. 5, 6). The application of thermal excitations also induces a similar topological-phase transition from the skyrmion state to a uniform ferroelectric state, with a phase-field estimated critical temperature of ~700 K. Experimentally, such phase transitions can be inferred from the presence (skyrmion phase, $N_{\mathrm{Q}} = 1$) or absence (trivial topological phase, $N_{\mathrm{Q}} = 0$) of intensity in the side-lobe satellites in the electric-field- (Fig. 4d-g) or temperature- (Fig. 4h and Extended Data Fig. 10) dependent RSMs. The satellite peaks arising from the skyrmions disappear, respectively, at 1500 kV/cm and at ~600 K, indicating that the topological number switched from +1 to 0 (Fig. 4, Extended Data Fig. 10); which, again, agrees qualitatively with the theoretical expectations. The field-driven change to the skyrmion is due to the shrinkage

of the volume of the domain with a polarization opposite to the external electric field. For a critical field, the domain will collapse and the transition to a monodomain state is completed. Right before the transition, a singularity appears: the stereographic projection of the dipole pattern does not completely wrap the unit sphere. That is exactly the point where the skyrmion number changes from +1 (non-trivial topological structure) to 0 (trivial case in the monodomain configuration). Finally, such a field/temperature driven topological-phase transition bears resemblance to that in other magnetic topological structures.[4,34,35,36,37]

Probing skyrmion dynamics with time dependent capacitance

To further understand the reversible evolution of these structures under applied fields, the temporal evolution of the skyrmion ground state can be probed by perturbing it with electric-field pulses that drive the system to a uniform-polar state and then measuring the time-dependent evolution back to the skyrmion state (Fig. 5, Supplementary Fig. 9, 10, and Methods). Here, we focus on two sets of measurements. The first focuses on applying strong, unipolar pulses (U_1 and U_2) with varying lengths of delay time (t_d) between the pulses. We measure the current that flows in the capacitor during the application of U_1 (*i.e.*, I_1), then allow possible relaxation to occur during t_d, and finally measure the current that flows during the application of U_2 (*i.e.*, I_2). Taking the difference I_1-I_2 for various t_d provides a time-dependent measure of the amount of relaxation after the poling process. For short-delay times ($t_d \lesssim 10$ μs; Fig. 5a, Supplementary Note 4), the parent 50-nm-thick $PbTiO_3$ film (data here at t_d = 200 ns, Fig. 5b, c), a flat, zero response corresponding to stable, poled ferroelectric behavior is observed. On the other hand, similar experiments for the superlattices with skyrmions (data here at t_d = 200 ns, Fig. 5d) reveal a transient peak suggesting that there is a relaxation process different from what is observed in a

300 classical ferroelectric based on the same material (data at other short t_d values is also provided,
301 Supplementary Fig. 10).

302 To further understand the relaxation processes, and in particular, reveal the time scales
303 over which these processes persist, we carried out similar experiments with progressively longer
304 t_d. Upon transitioning to long-delay times (10 μs $\lesssim t_d \lesssim$ 1 s, Fig. 5e and Supplementary Note 4),
305 the parent 50-nm-thick $PbTiO_3$ film (data here at t_d = 1 s, Fig. 5f-g), a flat, zero response
306 corresponding to a stable, poled ferroelectric behavior is once again observed. Likewise, similar
307 experiments for the superlattices exhibiting the skyrmion structures reveal a flat, zero response
308 suggesting the relaxation process has been completed within 1 s (data here at t_d = 1 s, Fig. 5h and
309 Supplementary Fig. 10).

310 Thus far, the observations suggest that (not surprisingly) the single-layer parent
311 ferroelectric film remains stable in whatever state it is electrically poled into, while the
312 superlattices exhibiting skyrmion structures are found to exhibit relaxation processes. This could
313 correspond to classical back-switching (*i.e.*, the applied bias pushes the skyrmion into a uniform
314 polar state which then relaxes back to a classical up-and-down-poled domain structure) or could
315 indicate an exotic relaxation back towards the skyrmion structure. To differentiate between these
316 two cases, a second set of experiments, wherein we apply a preset-pulse V opposite to U_1 and U_2
317 while focusing on long t_d (Fig. 5i and Supplementary Note 4), allows us to make this distinction.
318 When such an experiment is completed for the parent 50-nm-thick $PbTiO_3$ film (data here at t_d =
319 1 s, Fig. 5j-k), a non-zero response, corresponding to what is expected for a stable, poled
320 ferroelectric behavior is observed. This is in contrast to the data for the long-delay time studies
321 without the preset pulse which shows no peak (Fig. 5g). On the other hand, similar experiments
322 for the superlattices exhibiting the skyrmion (data here at t_d = 1 s, Fig. 5l) reveal a small transient

peak suggesting the ability to switch the small remnant polarization of the superlattice (Supplementary Fig. 9). From other experiments (Fig. 5d and g), it appears that these superlattices are relaxing or back-switching within ~1 s; however, if this was true, we should have seen no peak in this preset-pulse experiment (Fig. 5l). Thus, this is indicative of a totally different relaxation process, *i.e.*, it cannot be explained simply by a classical back-switching of a ferroelectric, but instead suggests there is an exotic, time-dependent evolution of the emergent polarization state such that we can unravel and then re-establish reversibly.

Our work has demonstrated a direct relationship between the macroscopically measured dielectric permittivity and the microscopically imaged potential energy landscape. Application of an electric field drives the skyrmions into a uniform polar state in a reversible way with an accompanying large tunability of the permittivity as well as a corresponding topological phase transition, which is analogous to what is observed in the case of magnetic skyrmions and their magnetic field driven evolution into a uniform magnetic state. The microscopic nature of this reversible recovery of the skyrmion state should be a matter of great interest for future studies.[38] Future electric field dependent dielectric spectroscopy measurements extending into the IR combined with new theory can help connect the frequency dispersion of the dielectric permittivity to the microscopic details of the skyrmion ensemble. The production of such a steady-state negative capacitance and large field-tunable response has promise for high frequency electronic applications.

[1] Das, S et al. Observation of room temperature polar skyrmions. *Nature* **568**, 368-372 (2019).

[2] Yadav, A. K. et al. Spatially Resolved Steady State Negative Capacitance. *Nature* **565**, 468-471 (2019).

[3] Kosterlitz, J. M. and Thouless, D. J., Ordering, metastability and phase transitions in two-

dimensional systems, *J. Phys. C: Solid State Phys*. **6,** 1181-1203 (1973).

[4] Nagaosa, N. and Tokura, Y., Topological properties and dynamics of magnetic skyrmions. *Nat. Nanotechnol*. **8**, 899-911 (2013).

[5] Rößler, U.K., Bogdanov, A.N., & Pfleiderer, C. Spontaneous skyrmion ground states in magnetic metals. *Nature* **442**, 797-801 (2006).

[6] Mühlbauer, S., Binz, B. Jonietz, F., Pfleiderer, C., Rosch, A., Neubauer, A., Georgii, R., and Böni, P. Skyrmion Lattice in a Chiral Magnet. *Science* **323**, 915-919 (2009).

[7] Nahas, Y., Prokhorenko, S., Louis, L., Gui, Z., Kornev, I. & Bellaiche, L. Discovery of stable skyrmionic states in ferroelectric nanocomposites. *Nat. Commun.* **6**, 8542 (2015).

[8] Zhang, Q. et al. Nanoscale bubble domains and topological transitions in ultrathin ferroelectric films. *Adv. Mater.* **29**, 1702375 (2017).

[9] Gregg, J. M. Exotic domain states in ferroelectrics: searching for vortices and skyrmions. *Ferroelectrics* **433**, 74–87 (2012).

[10] Naumov, I. I., Bellaiche, L. & Fu, H. Unusual phase transitions in ferroelectric nanodisks and nanorods. *Nature* **432**, 737–740 (2004).

[11] Salahuddin, S. and Datta, S. Use of negative capacitance to provide voltage amplification for low power nanoscale devices, *Nano Lett.* **8**, 405-410 (2008).

[12] S. Salahuddin and S. Datta, "Can the subthreshold swing in a classical FET be lowered below 60 mV/decade?," in Electron Devices Meeting, 2008. IEDM 2008. IEEE International, pp. 1–4, IEEE, 2008.

[13] Theis, T.N. and Solomon, P. M. It's time to reinvent the transistor!, *Science*, **327**, 1600-1601 (2010).

[14] Zubko, P. et al. Negative capacitance in multidomain ferroelectric superlattices. *Nature* **534**, 524-528 (2016).

[15] Appleby, D. J. R., Ponon, N. K., Kwa, K. S.K., Zou, B., Petrov, P. K., Wang, T., Alford, N. M., and O Neill, A., Experimental observation of negative capacitance in ferroelectrics at room temperature, *Nano Lett*., **14**, 3864-3868 (2014).

[16] Íñiguez, J., Zubko, P., Luk'yanchuk, I., Cano, A., Ferroelectric negative capacitance. *Nat. Rev. Mater.* 4, 243–256 (2019).

[17] Hoffman, M. et al. Unveiling the double-well energy landscape in a ferroelectric layer. *Nature* **565**, 464-467 (2019).

[18] Bratkovsky, A.M., Levanyuk. A.P. Depolarizing field and "real" hysteresis loops in nanometer-scale ferroelectric films. *Appl. Phys. Lett.* **89**, 253108 (2006).

[19] Wang, X. et al, Van der Waals negative capacitance transistors. *Nat. Commun.* **10**, 3037 (2019).

[20] Lines, M. E. & Glass, A. M. Principles and Applications of Ferroelectrics and Related Materials (Clarendon Press, Oxford, 1977)

[21] Wu, X., Yang, E. S., and Evans, H. L. Negative capacitance at metal-semiconductor interfaces. *Journal of Applied Physics* **68**, 2845-2848 (1990).

[22] Hoffman, M. et al, Ferroelectric negative capacitance domain dynamics. *J. Appl. Phys.* **123**, 184101 (2018).

[23] Damodaran, A. R. et al. Large polarization gradients and temperature-stable responses in compositionally-graded ferroelectrics. *Nat. Commun.* **8**, 14961 (2017).

[24] D. O'Neill, D., Bowman, R.M and Gregg, J.M. Dielectric enhancement and Maxwell–Wagner effects in ferroelectric superlattice structures. *Appl. Phys. Lett.* **77**, 1520-1522 (2000).

[25] Catalan, G., D. O'Neill, D., Bowman, R.M and Gregg. J.M. Relaxor features in ferroelectric superlattices: A Maxwell–Wagner approach. *Appl. Phys. Lett.* **77**, 3078-3080 (2000).

[26] Arai, H. *et al,* Fundamental Characteristics of Superconducting Fault Current Limiter Using LC Resonance Circuit. IEEE Transactions on Applied Superconductivity 16, 642-645 (2006)

[27] I. Luk'yanchuk *et al*. Electrodynamics of ferroelectric films with negative capacitance. Phys. Rev. B **98**, 024107 (2018).

[28] Kamba, S., Bovtun, V., Petzelt, J., Rychetsky, I., Mizaras, R., Brilingas, A., Banys, J., Grigas, J. and Kosec, M. Dielectric dispersion of the relaxor PLZT ceramics in the frequency range 20 Hz-100 THz. J. Phys.: Condens. Matter **12**, 497-519 (2000).

[29] Bovtun, V.; Veljko, S.; Savinov, M.; Pashkin, A.; Kamba, S.; Petzelt, J. Comparison of the Dielectric Response of Relaxor $PbMg_{1/3}Nb_{2/3}O_3$ Ceramics and Single Crystals. Integrated Ferroelectrics **69**, 3–10 (2005).

[30] Kittel, C. Introduction to Solid State Physics (Wiley, Hoboken, 1966)

[31] Watanabe, Y. in Ferroelectric Thin Films: Basic Properties and Device Physics for Memory Applications (eds Okuyama, M. & Ishibashi, Y.) 177–199 (Springer, Berlin, 2005).

[32] Zubko, P., Stucki, N., Lichtensteiger, C., and Triscone, J.-M., X-Ray Diffraction Studies of 180º Ferroelectric Domains in $PbTiO_3/SrTiO_3$ Superlattices under an Applied Electric Field. *Phys. Rev. Lett.* **104**, 187601 (2010).

[33] Boulle, A., Infante, and Lemée, N. Diffuse X-ray scattering from 180 ferroelectric stripe domains: polarization-induced strain, period disorder and wall roughness. *J. Appl. Cryst*. **49**, 845–855 (2016).

[34] Okamura et al. Transition to and from the skyrmion lattice phase by electric fields in a magnetoelectric compound. Nat. Commun. **7**, 12669 (2016).

[35] Fujishiro *et al*. Topological transitions among skyrmion- and hedgehog-lattice states in cubic chiral magnets. Nat. Commun. **10**, 1059 (2019)

[36] Yang *et al*. Electric field driven evolution of topological domain structure in hexagonal manganites. Phys. Rev. B **96**, 144103 (2017)

[37] Zong *et al*. Evidence for topological defects in a photoinduced phase transition. *Nat. Phys.* **15** 27-31 (2019).

[38] Schulz, A., Ritz, R., Bauer, A., Halder, M., Wagner, M., Franz, C., Pfleiderer, C., Everschor, K., Garst, M., and Rosch, A. Emergent electrodynamics of skyrmions in a chiral magnet. Nature Physics **8**, 301-304 (2012).

The author to whom correspondence: S.D (sujitdas@berkeley.edu) or R.R. (rramesh@berkeley.edu)

Acknowledgements

This work is supported by the Quantum Materials program from the Office of Basic Energy Sciences, US Department of Energy (DE-AC02-05CH11231). M.A.P.G. and J.I are funded by the Luxembourg National Research Fund through the CORE program (Grant FNR/C15/MS/10458889 NEWALLS). J.W.F., V.A.S.. H.W. and L.W.M. acknowledge support from the U.S. Department of Energy, Office of Science, Office of Basic Energy Sciences, under Award Number DE-SC-0012375 for the development and study of ferroic heterostructures. The phase-field simulation effort at Penn State is supported as part of the Computational Materials Sciences Program funded by the US Department of Energy, Office of Science, Basic Energy Sciences, under Award Number DE-SC0020145 and the Extreme Science and Engineering Discovery Environment (XSEDE) cluster, which is supported by National Science Foundation grant number ACI-1548562, and specifically, it used the Bridges system, which is supported by NSF award number ACI- 1445606, at the Pittsburgh Supercomputing Center (PSC), under the allocation DMR170006. F.G.O, P.G.F. and J.J. acknowledge financial support from the Spanish Ministry of Economy and Competitiveness through grant number FIS2015-64886-C5-2-P and PGC2018-096955-B-C41, and P.G.F. acknowledges support from Ramón y Cajal grant No.

RyC-2013-12515. V.A.S., M.R.M, S.D., H.W., Z.Z., J.W.F. and H.Z. acknowledge use of the Advanced Photon Source, a U.S. Department of Energy (DOE) Office of Science User Facility operated for the DOE Office of Science by Argonne National Laboratory under Contract No. DE-AC02-06CH11357. V.A.S. and H.W. would like to thank to Qian Li and Samuel Marks for kind assistance in operating the XNOM station at 7-ID-C beamline of APS. Y.T.S. and D.A.M. acknowledge support from the AFOSR Hybrid Materials MURI, under award number FA9550-18-1-0480. We acknowledge the electron microscopy facility from the National Science Foundation (DMR-1719875 and DMR-1429155). E.J.M., C.J.L., N.D.O. acknowledge to J.C. Booth for establishing the high frequency testing facility at NIST, funding E.J.M., and developing the original on-wafer techniques.

Author Contributions

S.D. and R.R. designed the experiments. S.D. carried out the synthesis and characterization of trilayers and superlattice samples. S.D. carried device fabrication on this samples and S.D. and S.Saremi performed all macroscopic electrical measurements. Y.T.S. performed EMPAD characterization of the samples under the supervision of D.A. M. M. A. P. G, F.G.O, P.G.F, J. Í. and J.J. completed the second-principles simulations. Z.H. performed and analyzed phase-field calculations for these samples. V.A.S., M.R.M. and S.D. did the reciprocal space map studies of these samples using lab x-ray diffraction and synchrotron X-ray diffraction. V.A.S. carried out the electric field dependent reciprocal space map studies of these samples using synchrotron X-ray diffraction. E.P. and S.D. performed electric field dependent of pulse dynamics. E.J.M designed the layout, fabricated the in-plane devices and performed the microwave measurements, analyzed the data and wrote microwave section. N.D.O. and A.M.H. supervised the microwave research and N.D.O. wrote the algorithms that calibrated and processed the data, wrote the analysis tools. C.J.L. wrote the algorithms that generated the layout, optimized the devices performance, and calibrates and processes the data. S.D. Z.H. V.A.S., J.J., L.Q.C., and

R.R. analyzed the data and co-wrote the manuscript. R.R., L.Q.C., L.W.M., S. Salahuddin and J.J. supervised the research. All authors contributed to the discussion and manuscript preparation.

Competing financial interests

The authors declare no competing financial interests.

Figure 1| Macroscopic demonstration of stabilization in the negative capacitance of polar skyrmion. a, The dielectric permittivity as a function of electric field (applied voltage divided by the thickness of the sample) for $[(SrTiO_3)_{16}/(PbTiO_3)_{16}]_8$, $[(SrTiO_3)_{16}/(PbTiO_3)_{16}]_5$, $[(SrTiO_3)_{16}/(PbTiO_3)_{16}]_3$ superlattice and $(SrTiO_3)_{16}/(PbTiO_3)_{16}/(SrTiO_3)_{16}$ trilayer which is in skyrmion states compared to its constituents (50nm $SrTiO_3$ and 50 nm-thick $PbTiO_3$ layer). The horizontal dotted yellow line shows the effective permittivity at zero field (~37) from the series combination of effective 50nm $SrTiO_3$ and 50nm $PbTiO_3$ layers. Inset: schematic of the sample measurement geometry. **b,** Left axis: experimentally measured effective dielectric permittivity (blue dots) as a function of electric field manifests itself in the enhancement of dielectric permittivity of the $[(SrTiO_3)_{16}/(PbTiO_3)_{16}]_8$ superlattice compared to the series permittivity (horizontal dotted yellow line) at zero field (~37). An enhancement in permittivity of almost ~20X is observed compared to this threshold, caused by a stabilized negative capacitance

(permittivity) in the $PbTiO_3$ layer. Right axis: The normalized dielectric permittivity calculated from phase field (red dashed) and second-principles (green dashed) simulations closely resembles with the experimentally measured normalized electric-field dependence permittivity (blue dots). The results have been rescaled and the normalization is done with respect to the zero-field value.

Figure 2| Phase field, second-principles and macroscopic calculations of negative permittivity of the skyrmion structure at 300 K in a $[(SrTiO_3)_{16}/(PbTiO_3)_{16}]_8$ superlattice. a, Left: second-principles calculations of the skyrmion structure. Right: phase field simulated spatial map of the permittivity of the central $PbTiO_3$ layer of the skyrmion and presents the evidence of negative local permittivity regions (blue contrast). Second principles calculations of the two-dimensional distribution of **b,** the inverse of the dielectric permittivity and **c,** the susceptibility at the central plane of $PbTiO_3$, that shows the Bloch-like skyrmion texture. Both are computed as in Ref.2, and are color coded with the key at right. Both b and c are overlaid by the polarization vectors. The arrows represent the components of the polarization in the *xy*-plane of the skyrmion. **d,** Macroscopic illustration of our $PbTiO_3$–$SrTiO_3$ system (details in method) (left) and it's corresponding circuit diagram (right). R_{ext} describes some external resistance of the circuit leading up to the thin film capacitor, *e.g.* from the electrodes. **e,** Calculations of the permittivity of the skyrmion wall (ε_3) as a function of ε_1 and ε_2 based on the model described in

(d). A 3-dimensional plot of the inter-dependence between ε_1, ε_2 and ε_3, constrained by the effective dielectric permittivity, ε_{eff}, to be 800 (to match the experimental results in Fig.1a, Supplementary Note 1); The permittivity of the skyrmion wall is always negative except for non-reasonable values of the permittivity of the $SrTiO_3$ and $PbTiO_3$ layers: for example, identified by the data points with fictitious permittivities. These fictitious scenarios are unlikely since it would mean that both $SrTiO_3$ and $PbTiO_3$ have a significantly enhanced permittivity compared to that in the bulk. **f,** A section of the phase space in (e), showing calculations of the permittivity of the skyrmion wall (ε_3) as a function of ε_1 and ε_2 specifically for values of the $SrTiO_3$ and $PbTiO_3$ layer permittivities from 0-300 (which is a reasonable range for thin films), showing that the wall permittivity is negative over the entire range.

Figure 3| Measurement of local polarization, electric field, and local potential energy of the polar skyrmion using SCBED. a, A cross-sectional HAADF-STEM image of the skyrmions in the $PbTiO_3$ layer. **b**, Polarization and **c,** electric field vector map of the skyrmion measured using SCBED for the cross-section geometry (*x*-*z* plane), where we can access the cross-section of the Neél component (blue box) and the Bloch component (red box) from the skyrmion. The out-of-plane polarizations are separated by in-plane Bloch chiral domain walls (dark regions). The color wheel hue (saturation) corresponds to the direction (magnitude) of the in-plane component of the ferroelectric polarization. **d**, Variation in the z components of local polarization (P_z; blue curve) and electric field (E_z; orange curve) along a horizontal line profile drawn through the center of a polar skyrmion, as indicated by dashed lines in b and c. **e**, Local potential energy estimated from the variation in P_z and E_z along the same line. Regions around the skyrmion walls (arrowed) do

have a local energy higher than the surroundings with a negative curvature ($(\partial^2 U)/(\partial P^2) < 0$), indicating local negative permittivity.

Figure 4| Electric field control of topological phase transition of polar skyrmion of $[(SrTiO_3)_{16}/(PbTiO_3)_{16}]_8$ superlattice. a-c, Phase field simulations show the shrinking of the diameters of the skyrmions under electric field (left to right), and ultimately the entire sample becomes uniformly ferroelectric ~ 1500 kV/cm. **d-e,** Electric field dependent reciprocal space maps shows the systematic disappearance of the satellite peaks (side-lobes, which correspond to the skyrmions) with electric field. **f,** Intensity profile vs. electric field shows disappearance of the skyrmion peaks around ~1500 kV/cm (right). **g,** Dependence of topological number under the electric field. At ~ +1500 kV/cm topological number flip from +1 to zero indicating the topological skyrmion phase transfer to trivial single domain state. Topological number from a phase-field simulation (red symbols and lines) of the same $(SrTiO_3)_{16}/(PbTiO_3)_{16}$ superlattice, which closely match the experimental observations (green symbols and lines). **h,** Dependence of topological number under the temperature. Around ~600K topological number flip from +1 to

zero indicating the topological skyrmion phase transfer to ferroelectric mono-domain state. This observation is slightly different from the phase field simulation due the strain relaxation (red symbols and line).

Figure 5| Generation of a transient state with time dependent capacitance under out-of-plane measurement geometry of the skyrmion. a, Schematic of two unipolar pulses (U_1 and U_2) applied to the sample with short delay time, t_d, between pulses. U_1 poles the sample to the uniform polarization state. Zero field is applied for time t_d, during which, the system relaxes. We monitor the difference in current response to U_1 and U_2 ($I_1 - I_2$) to reveal a transient state after initial poling. **b,** shows the expected difference ($I_1 - I_2$) for a ferroelectric with (dashed green) and without back-switching (solid green). **c,** $I_1 - I_2$ for the parent ferroelectric (50 nm $PbTiO_3$ layer), indicating a stable polarization. **d,** The superlattice with a notable peak, suggesting the existence of a relaxation process. To probe the timescale of relaxation we perform the experiment diagrammed in **e.**, changing to a long-time delay, t_d. Expectation for a classical

ferroelectric with complete back switching (long dash), partial back switching (short dash) and stable ferroelectric polarization (solid) is shown in **f**. **g,** As expected, the parent 50nm $PbTiO_3$ layer shows a flat line, i.e., stability. **h,** Notably, the superlattice also shows a flat difference indicating that relaxation has completed at this timescale (t_d = 1s shown). Finally, we perform the experiment diagrammed in **i.** where we apply a preset pulse down pulse (V) and monitor $I_1 - I_2$ for long t_d. **j,** shows expectation from a ferroelectric, a switchable, stable polarization (solid line). **k,** The parent 50 nm $PbTiO_3$ layer shows a large signal coming from the switchable remnant polarization. **l,** The $I_1 - I_2$ for the skyrmion sample, which importantly shows a distinguishable signal. This, in conjunction with the data in **d.** and **h.** indicates that the origin of the relaxation seen in the skyrmion sample is not back-switching of the small remnant polarization but rather a new mechanism originating from the polar skyrmion structure.

METHODS

Sample preparation using RHEED-assisted pulsed-laser deposition

n-$SrTiO_3$/*n*-$PbTiO_3$/*n*-$SrTiO_3$ trilayers (*n*- is the number of monolayers) and $[(PbTiO_3)_n/(SrTiO_3)_n]_m$ (*n*- is the number of monolayers, *n*=8-16, *m*=3-8) superlattices were sandwiched by conducting 10 nm bottom $SrRuO_3$ and 60 nm top $SrRuO_3$. Trilayer and the superlattices were synthesized on TiO_2-terminated single-crystalline $SrTiO_3$ (001) substrates via reflection high-energy electron diffraction (RHEED)-assisted pulsed-laser deposition (KrF laser). The $PbTiO_3$ and the top $SrTiO_3$ were grown at 600 °C in 100 mTorr oxygen pressure. Growth temperature and oxygen pressure for the bottom $SrRuO_3$ layer were 700°C and 50 mTorr, respectively. For the top $SrRuO_3$ layer the corresponding parameters were 600°C and 100mTorr. For all materials, the laser fluence was 1.5 J/cm^2 with a repetition rate of 10 Hz. RHEED was

used during the deposition to ensure the maintenance of a layer-by-layer growth mode for both the $PbTiO_3$ and $SrTiO_3$. The specular RHEED spot was used to monitor the RHEED oscillations. After deposition, the superlattices were annealed for 10 minutes in 50 Torr oxygen pressure to promote full oxidation and then cooled down to room temperature at that oxygen pressure.

Structural analysis

Laboratory-based X-ray diffraction: Structural characterization of the trilayer and superlattices were carried out using an Panalytical X'Pert Pro X-ray Diffraction (XRD) diffractometer with Cu-K_α radiation (λ = 1.5405 Å). The high crystalline quality of the films, and the smooth nature of the interfaces were confirmed from θ-2θ symmetric XRD scans around the 002 reflection, which show strong superlattice peaks and Laue oscillations (not shown).

Synchrotron X-ray diffraction: In order to obtain a comprehensive picture of the structure, of the skyrmion in the trilayers and superlattices, as well as information on the in-plane and out-of-plane ordering and temperature dependent skyrmion structures, further structural characterization was performed using synchrotron-based XRD with monochromatic hard X-ray beams at 10 keV to 25 keV at the 33-BM-C, 33-ID-B, 7-ID-C and 12-ID-B beamlines of the Advanced Photon Source (APS), Argonne National Laboratory, USA. The Huber and Newport diffractometers used at APS allows us to determine the orientation of our crystals reliably, and to obtain 3-dimensional reciprocal space mappings based on rocking scan sampling with high angular accuracy. The high flux from the synchrotron X-ray source delivered at these beamlines allows one to detect the weak diffracted intensities arising from the lattice modulations associated with the polar-skyrmion bubbles present in the $(PbTiO_3)_n/(SrTiO_3)_n$ superlattices.

Macroscopic capacitance measurement

Out-of-Plane Measurements: In order to measure the electrical properties of the superlattices circular capacitor structures of 25 μm, 50 μm, 100 μm diameter were fabricated using pulsed laser deposition followed by photolithography and etching. The fabrication is comprised of three processes: a) etching, b) lift-off and c) shadow mask deposition. At first photolithography was used to define the photoresist layer. Dry etching was carried out by Ar ion beam milling at 1×10^{-4} Torr Ar pressure at a rate of 6 nm/min to remove the top electrode layer. Temperature dependent small signal ac permittivity was measured using an E4990A Impedance Analyzer using an a.c. excitation voltage of 10mV at various frequencies.

In-plane Measurements: A transmission-line approach was used to measure the in-plane dielectric properties of a $[(PbTiO_3)_{16}/(SrTiO_3)_{16}]_8$ superlattice at microwave frequencies from 100 MHz to 10 GHz. To perform these measurements, an array of eight gold co-planar waveguide (CPW) transmission lines ranging in length from 0.42 mm to 6.60 mm were patterned on the surface of the superlattice film using standard lift-off fabrication techniques (Extended Data Fig. 6a). The center conductor of the CPWs was 20 μm wide and was separated from 150 μm-wide ground planes by a 5 μm wide gap. An identical pattern was also fabricated on a bare $SrTiO_3$ (001) substrate for reference. The dimensions of the devices were measured using optical microscopy and profilometry, and the conductivity of the gold was obtained from DC resistance measurements.

The scattering (S-) parameters of the transmission line devices were then measured at room temperature from 100 MHz to 10 GHz using a vector network analyzer (VNA) at a power

of -15 dBm and an IF bandwidth of 30 Hz. The VNA was calibrated using custom-fabricated on-wafer calibration standards with device geometries consistent with the devices on the superlattice film and bare substrate. The NIST StatistiCal software package was used to implement the multiline-TRL algorithm[39,40] to extract accurate estimates of the propagation constant, γ, from the S-parameter measurements of the CPWs on the superlattice film and bare substrate. The propagation constant is related to the distributed circuit parameters of the CPW by the relationship $\gamma = \sqrt{R + i\omega L}\sqrt{G + i\omega C}$, where R, L, G, and C are the distributed resistance, inductance, conductance and capacitance per unit length, respectively, and ω is the angular frequency. These circuit parameters are related to the geometries and material properties of the metal layers comprising the CPW, and the surrounding dielectric layers, which are probed by electric fields generated in the devices during measurement (Extended Data Fig. 6b). If R and L are known, C and G, which are proportional to the real and imaginary parts of the effective permittivity, respectively, can be extracted from γ. In the devices on the superlattice film chip, the in-plane electric fields interact with both the superlattice film and the substrate, therefore some portion of the overall measured C and G can be attributed to the permittivity of the film (C_{FILM}, G_{FILM}), and to the permittivity of the substrate (C_{SUB}, G_{SUB}) as illustrated in the stylized circuit model for these transmission lines (Extended Data Fig. 6c). The measurement of the bare substrate is used to aid in separating these contributions to the overall measurement. Finite element simulations of the device structures incorporating the measured dimensions and metal properties were generated and validated by comparison to known devices. These simulations are first used to obtain the R and L values for the CPW devices in order to extract C and G, and finally are used to obtain the mapping function relating C and G to the real (ε') and imaginary (ε'') parts of the permittivity, respectively.

In-situ electric field dependent structural measurements

Synchrotron X-ray diffraction measurements as a function of electric field (applied voltage divided by the thickness of the sample) were conducted at the 7-ID-C, 32-ID-B and 12-ID-B beamlines at APS using $(PbTiO_3)_n/(SrTiO_3)_n$ superlattice samples deposited on (100) $SrTiO_3$ substrates, n=16, 20 and total superlattice thickness of ~ 100 nm. By employing capacitor device geometry with superlattice sandwiched between $SrRuO_3$ electrodes grown at the substrate interface and on top of the superlattice stack, additional *in-situ* electric-field-dependent measurements of superlattices were performed at 7-ID-C and 32-ID-B beamlines. In a first device geometry used at sector 32-ID-B, the incident X-ray beam at 10 keV was focused using two Kirkpatrick-Baez (KB) mirrors to a spot of ~ 30 μm x 90 μm on the top electrode of a capacitor device with a lateral size of 150 μm x 150 μm. To study the effect of out-of-plane electric field, a constant dc voltage was applied to the capacitor device, while the intensity of various peaks was monitored with a gated area detector, which acquired the distribution of scattered X-ray intensity in reciprocal space, followed by reciprocal space mapping reconstruction. Device to device data reproducibility was additionally checked at sector 7-ID-C using several capacitor devices with 25 μm diameter and a 11 keV X-ray beam focused by a zone-plate to ~ 1 μm x 1 μm on the top of the capacitors. On these smaller capacitors, the electric field application was initiated using a sharp Pt tip of a few nm's in size placed in contact with the top electrode under a nanoscale probe imaging station called X-ray Scanning Near-field Optical Microscope (XSNOM).[41]

Phase-field modeling

To predict and understand the structures and responses of the polar skyrmions under applied electric and thermal stimuli, phase-field simulations[42,43] were performed for the $(PbTiO_3)_{16}/(SrTiO_3)_{16}$ superlattice on a $SrTiO_3$ substrate by evolving spatial distributions of polarization vector $\vec{P}$, strain, and electric potential (and thus electric field). [1, 2, 43]

$$\frac{\partial P_i}{\partial t} = -L\frac{\delta F}{\delta P_i} (i=1, 3)$$

where t is the simulation time step, and L is the kinetic coefficient related to the bulk domain wall mobility.

The total free energy F of the superlattice contains contributions from mechanical, electrostatic, Landau chemical and polarization gradient energies:

$$\mathrm{F} = \int_V \left(f_{mech} + f_{elec} + f_{Land} + f_{grad}\right) dV$$

The detailed expressions of the energy densities and the material parameters can be found elsewhere.[44,45] The simulation cell is discretized into 3-Dimensional grids of $200 \times 200 \times 350$, with each grid representing 0.4 nm. Periodic boundary conditions are applied along the in-plane dimensions while a superposition scheme[44] is imposed along the thickness dimension which is composed of 30 grids of substrate, 288 grids of thin film layers (which is consisting of repeating units of 16 $PbTiO_3$ layers and 16 $SrTiO_3$ layers) and 32 grids of vacuum. The thin film boundary condition is applied where it is stress free on the top of the film and the displacement is zero on the bottom of the substrate sufficiently far away from the substrate/thin film interface.[43] An iteration-perturbation method is used to account for the elastic inhomogeneity of the two materials.[45]

The local electric potential φ can be obtained by solving the Poisson's equation[44]: $\varepsilon_0 K_{ij} \frac{\partial^2 \varphi}{\partial x_i x_j} = P_{i,i}$, where ε_0 is the permittivity of vacuum, K_{ij} is the background dielectric constant.[42] The electric field E_i can be expressed by the gradient of the electric potential, i.e., $E_i = -\nabla_i \varphi$. A close-circuit electric boundary condition[46] is used with the electric potential both at the bottom and top of the thin film set to be zero or a specified applied potential. The polar skyrmion array[1] is stabilized at room temperature, starting from initial random noise, which is used for the follow-up calculations. The macroscopic dielectric constant at the given electric potential bias is calculated by giving small potential perturbations: $\varepsilon_{33} = \frac{\Delta < P_3 > d}{\varepsilon_0 \Delta \phi} + K_{33}$, d is the thickness of the thin film. While the spatially resolved local permittivity[3] is defined as: $\varepsilon_{33} = \frac{\Delta P_3}{\varepsilon_0 \Delta E_3} + K_{33}$. The thermal stability of the polar skyrmion is also investigated in the temperature range of 300 K to 800 K. Since, $PbTiO_3$ and $SrTiO_3$ have similar thermal expansion coefficients, the substrate strain is assumed to be constant across the whole temperature range. The lower bound of the transition temperature is estimated by adding a 0.05% relaxation of the substrate strain (which is the uncertainty of the measurement). The switching kinetics are also studied with an applied field in the range from -1500 kV/cm to +1500 kV/cm.

Second-principles calculations

The second-principles simulations have been performed using the same methodology presented in previous works[1,47,48,49] as implemented in the SCALE-UP package.[47] The interactions inside the $PbTiO_3$ or $SrTiO_3$ are described using the potentials for the bulk materials.[48] These potentials give qualitatively correct descriptions for the lattice dynamical properties and structural phase transitions of both materials. Then, we treat the interactions at the interface between $PbTiO_3$ and

$SrTiO_3$ assuming a simple numerical average for the interactions of the ions pairs touching or crossing the interface. The main effect of the stacking is electrostatic wherein long-range dipole-dipole interactions are governed by a bare electronic dielectric constant ε_∞ that is taken as a weighted average of the first-principles results for bulk $PbTiO_3$ ($8.5\varepsilon_0$) and $SrTiO_3$ ($6.2\varepsilon_0$), with weights reflecting the composition of the superlattice. To preserve the electrostatic energy within each material as close as possible to the bulk parent compounds, the Born effective charge tensors of the inner atoms were rescaled by $\sqrt{\varepsilon_\infty}/\varepsilon_\infty^{ABO_3}$ (where ABO_3 stands for $PbTiO_3$ or $SrTiO_3$ depending on the layer).

The second-principles parameters of both materials were fitted from density functional theory imposing a hydrostatic pressure of -11.2 GPa to counter the underestimation of the local density approximation (LDA) of the cubic-lattice constant that was taken as the reference structure. We impose an epitaxial constraint assuming in-plane lattice constants of a=b=3.901 Å, forming an angle γ=90°, which corresponds to a $SrTiO_3$ (001)-oriented substrate.

Following this strategy, we are able to construct models for superlattices with arbitrary n stacking. For the simulations, we used periodically repeated supercells that contain 20×20 elemental perovskites units in-plane, and one full superlattice period in the out-of-plane direction. To solve the models, we have used standard Monte Carlo and Langevin molecular-dynamics methods; at low temperature only random configurations along the Markov chains that produce a lowering in the energy are accepted. By following this procedure as an equivalent to structural relaxations we find the ground state. The local polarizations were obtained within a linear approximation, computing the product of the atomic displacements from the reference structure, that correspond to the ideal cubic perovskite, times the Born effective charge tensor divided by the volume of the unit cell. The skyrmion number, N_{SK}, was obtained from the local

dipoles computing the normalized polarization field defined along each slice of 20×20×1 elemental perovskite unit in-plane of our supercell and solving the Eq. (1), obtaining a skyrmion number that corresponds to an integer number.[1,50]

Finally, the local dielectric constant and the electric susceptibilities were computed following the strategy presented in ref. 2. There the inverse of the dielectric constant was defined to be a measurement of the change in the local electric field with the variation of the electrical boundary conditions that sets the macroscale electric displacement vector. The normal component of the displacement electric field can be monitored by the external electric field. In the same spirit, the local electric susceptibilities measure the changes in the local polarization under the application of the same external electric field.

To compute the global dielectric permittivity, the skyrmion structure was relaxed under different external electric fields of increasing magnitude. The starting configuration for a given value of the external field was the relaxed structure obtained for the former field. After relaxation, the global polarization along the *z*-direction was averaged for the whole supercell. From the plot of P_z versus the external field, a fit to a Landau-type equation of state was performed, including up to five order terms. Finally, the global electronic susceptibility was estimated as $\epsilon_z = 1 + \frac{1}{\epsilon_0}\frac{\partial P_z}{\partial E_{\text{ext},z}}$.

SCBED for local potential energy measurement

Scanning convergent beam electron diffraction (SCBED) experiments were performed using an electron microscopy pixel array detector (EMPAD) in 4D-STEM and a TEM operated at 300 keV with 15 pA beam current, 2.0 mrad semi-convergence angle, having a probe of ~8 Å FWHM (full-width at half-maximum). The CBED patterns were captured by the EMPAD with

exposure time set to 1 ms per frame. The TEM specimen has a thickness of ~25 nm as determined by CBED simulations using EMPAD. Cross-sectional measurements enable access to the cross-section of the Bloch and the Neel component of the skyrmions away from the interfaces, where the technique is most robust.

Both ferroelectric polarization and electric field need to be measured independently and simultaneously to extract local potential energy. First, long-range electric fields can be reconstructed from the deflection of the entire CBED pattern due to the Lorentz force[29, 30]. For this study, we focused on the deflection of the (000) beam as there are fewer polarity effects. Secondly, due to dynamical diffraction effects, the polarization direction can be retrieved from the diffraction intensity differences of Friedel pairs, such as (100)/($\bar{1}$00) and (001)/(00$\bar{1}$) for the x and z component of polarity, respectively. We carefully selected local regions with minimal tilt and thickness variations, as these effects complicate the analysis and give rise to nontrivial artefacts.

Now that both electric field and polarization field are measured, we can thus calculate local potential energy of the system following the approach given in Ref. 2.

Based on the analysis (Fig.3), the potential energy has local maxima at the skyrmion domain walls, where the out-of-plane polarization (z component) was suppressed.

Probing the transient capacitance state

We apply a series of two identical, consecutive (U_1 and U_2 in Fig.4a) unipolar pulses with a pulse width of 10 μs to the sample. Each pulse generates a field of 1300kV/cm in the film. During each pulse, we monitor the current through the sample. The time delay between pulses is variable, given by t_d. During the delay time, no electric field is applied and the system begins to

relax to the ground (skyrmion) state. U_2 probes the capacitance *at the time of application,* and as such by varying t_d and comparing the currents I_1 and I_2 generated in the circuit in response to the pulses U_1 and U_2, we can probe the evolution of the sample back toward the ground state. Upon subtracting the response (*i.e.,* I_2) to pulse U_2 from the response (*i.e.,* I_1) to pulse U_1, we observe a discernable difference between the response to poling pulse (U_1) and the following pulse (U_2) (Fig.4). This difference is attributed to the formation of a transient capacitive state where the system is driven out of equilibrium (toward the uniform polarization state) and then relaxes back to the ground state. The difference between U_1 and U_2 is largest for short delay times, t_d, and decays with longer delay times, as is expected while the transient state decays. This difference could be attributed to back-switching of the small remnant polarization of the sample, however a similar experiment which includes a preset down pulse reveals that this cannot be the case (Fig. 5).

[39] Marks, R. B., A multiline method of network analyzer calibration. *IEEE Trans. Microw. Theory Tech.* **39**, 1205-1215 (1991).

[40] Williams, D. F., Wang, J. C. M. & Arz, U. An optimal vector-network analyzer calibration algorithm. *IEEE Trans. Microw. Theory Tech.* **51**, 2391-2401 (2003).

[41] Li, Q. *et al*. Simultaneous scanning near-field optical and X-ray diffraction microscopy for correlative nanoscale structure–property characterization. J. Synchrotron Rad. **26**, 1790-1796 (2019).

[42] Towns, J., Cockerill, T., Dahan, M., Foster, I., Gaither, K., Grimshaw, A., Hazlewood, V., Lathrop, S., Lifka, D., Peterson, G.D., Roskies, R., Scott, J.R. and Wilkens-Diehr, N. XSEDE: Accelerating Scientific Discovery. Computing in Science & Engineering. **16**, 62-74 (2014).

[43] Nystrom, N. A., Levine, M. J., Roskies, R. Z., and Scott, J. R. 2015. Bridges: A Uniquely Flexible HPC Resource for New Communities and Data Analytics. XSEDE Conference: Scientific Advancements Enabled by Enhanced Cyberinfrastructure 30, 1-8 (2015). https://doi.org/10.1145/2792745.2792775

[44] Chen, L.-Q., Phase-Field Method of Phase Transitions/Domain Structures in Ferroelectric. Thin Films: A Review. *J. Am. Ceram. Soc*. **91**, 1835-1844 (2008).

[45] Sheng, G., Li, Y.L., Zhang, J.X., A modified Landau–Devonshire thermodynamic potential for strontium titanate. *Appl. Phys. Lett.,* 96, 232902 (2010).

[46]Tagantsev, A. *et al.*, Landau Expansion for Ferroelectrics: Which Variable to Use? *Ferroelectrics,* **375**, 19-27 (2008).

[47] Wojdeł, J. C., Hermet, P., Ljungberg, M. P., Ghosez, P. & Íñiguez, J. First- principles model potentials for lattice-dynamical studies: general methodology and example of application to ferroic perovskite oxides. *J. Phys.: Condens. Matter* **25,** 305401 (2013).

[48] Wojdeł, J.C. and Íñiguez, J., Ferroelectric transitions at ferroelectric domain walls found from first-principles. *Phys. Rev. Lett.* **112**, 247603 (2014).

[49] Gonçalves, M. A. P. *et* al, Theoretical guidelines to create and tune electric skyrmion bubbles. *Science Advances* **5**, no. 2, eaau7023 (2019).

[50] B. Berg, B and Lüscher, M. Definition and statistical distributions of a topological number in the lattice O(3) σ-model, *Nucl. Phys. B* **190**, 412-424 (1981).

Data availability

All data supporting the findings of this study are available within the paper and/or are available from the authors upon reasonable request.

Extended Data Fig.1| Polar skyrmion structure in $[(SrTiO_3)_{16}/(PbTiO_3)_{16}]_8$ superlattice. a, Planar-view dark-field STEM imaging shows the widespread occurrence of nanometer-size (~8 nm) skyrmion formation along the [100] and [010] directions. **b,** Second-principles calculations of the skyrmion structure in the superlattice. The hedgehog-like skyrmion (Topological number +1) at the top and bottom interface between $SrTiO_3$ and $PbTiO_3$, and the Bloch-like skyrmion (topological number +1) at the central plane in $PbTiO_3$ are clearly visible. The arrows represent the normalized electric dipole moments.

Extended Data Fig.2| Synchrotron-based symmetric three-dimensional reciprocal space mapping about the (002) diffraction condition of the $SrTiO_3$ substrate. Reciprocal space mapping of **a,** $(SrTiO_3)_{16}$ /$(PbTiO_3)_{16}$/$(SrTiO_3)_{16}$ trilayer, **b,** $[(PbTiO_3)_{16}/(SrTiO_3)_{16}]_3$ superlattice, **c,** $[(PbTiO_3)_{16}/(SrTiO_3)_{16}]_5$ superlattice and **d,** $[(PbTiO_3)_{16}/(SrTiO_3)_{16}]_8$ superlattice. The satellite peaks along (100) direction (side-lobes; white arrow) which correspond to the skyrmions.

Extended Data Fig.3| Loss Tangent as a function of electric field. The loss tangent (tanδ) as a function of electric field for **a,** $[(SrTiO_3)_{16}/(PbTiO_3)_{16}]_8$ superlattice, **b,** $[(SrTiO_3)_{16}/(PbTiO_3)_{16}]_5$ superlattice, **c,** $[(SrTiO_3)_{16}/(PbTiO_3)_{16}]_3$ superlattice, **d,** $(SrTiO_3)_{16}/(PbTiO_3)_{16}/(SrTiO_3)_{16}$ trilayer which is in the skyrmion state compared to its constituents **e,** 50nm $SrTiO_3$ (brown) and **f,** 50 nm-thick $PbTiO_3$ layer.

Extended Data Fig.4| Measured out-of-plane dielectric permittivity as a function of electric field for the a, $[(SrTiO_3)_{16}/(PbTiO_3)_{16}]_8$ superlattice (skyrmion sample) compared with 50nm $SrTiO_3$ and 50 nm $PbTiO_3$ layers on $SrTiO_3$ (001) and **b,** $[(SrTiO_3)_{16}/(PbTiO_3)_{16}]_8$ superlattice (vortex sample) compared with 50nm $SrTiO_3$ and 50 nm $PbTiO_3$ layers on $DyScO_3$ (110) substrate. The enhancement of dielectric permittivity for the skyrmion sample ~ 20X larger compared to its series permittivity whereas it only ~ 9X for vortex samples.

Extended Data Fig.5| Out-of-plane dielectric permittivity as a function of frequency measured on three different devices. a, Capacitance vs Frequency of $[(SrTiO_3)_{16}/(PbTiO_3)_{16}]_8$ superlattice (superlattice total thickness: 100nm, capacitor size of the measurement: 25μm) compared with 50nm $PbTiO_3$ (orange), 50nm $SrTiO_3$ layers (brown) (capacitor size of the measurement: 25 μm) at electric field E=0 kV/cm and E=1000 kV/cm (light green). **b,** Tangent loss (Tanδ) vs Frequency of $[(SrTiO_3)_{16}/(PbTiO_3)_{16}]_8$ superlattice compared with 50nm $PbTiO_3$

(orange) and 50nm $SrTiO_3$ (brown) layers. It shows the Tanδ which is approximately an order of magnitude smaller than for samples which show Maxwell-Wagner (MW) effects in the literature (Ref. 24, 25). **c,** Dielectric permittivity vs Frequency of $[(SrTiO_3)_{16}/(PbTiO_3)_{16}]_8$ superlattice which is in the skyrmion state measured in three different capacitor devices compared with 50nm $PbTiO_3$ (orange) and 50nm $SrTiO_3$ (brown) layers at electric field E=0 kV/cm and E=1000 kV/cm (light green). **d,** Capacitance (left axis), permittivity (right axis) as a function of electric field of $[(SrTiO_3)_{16}/(PbTiO_3)_{16}]_8$ superlattice which is in the skyrmion state at 10kHz (blue), 100kHz (red) and 1MHz (green). The capacitance and permittivity change by ~ 4% over the measured frequency range. This reveals that the calculated negative permittivity from this macroscopic measurement is independent of measured frequency in this range.

Extended Data Fig.6| In-plane dielectric permittivity of $[(SrTiO_3)_{16}/(PbTiO_3)_{16}]_8$ superlattice at microwave frequencies from 100 MHz to 10 GHz. a, A schematic of co-planar Waveguide (CPW) transmission lines for microwave-frequency permittivity characterization. **b,** A cross-sectional view of the CPW illustrating the electric fields between the center conductor and ground planes. **c,** A circuit model of the CPW transmission line showing how the total measured capacitance of the transmission line (C) is comprised of a portion related to the permittivity of the $SrTiO_3$ substrate (C_{SUB}), and a portion related to the permittivity of the superlattice (C_{FILM}). **d,** The measured capacitance of the CPW transmission lines on the superlattice (purple), and $SrTiO_3$ substrate (red) are shown. Finite element simulations and the measurements of the bare $SrTiO_3$ substrate are used to analyze and isolate the portion of the total capacitance which is related to the permittivity of the superlattice (blue). **e,** The real part of the in-plane dielectric permittivity (left-hand y-axis) and the loss tangent (right-hand y-axis) are

determined from the capacitance and conductance measurements via a mapping function obtained from 2D finite element modeling of the CPW structures; **f,** Cole-Cole model of the in-plane complex permittivity of the superlattice from 100 MHz to 10 GHz (Supplementary Note 2).

Extended Data Fig. 7| Phase field simulation of the switching dynamics of skyrmions under different externally applied fields. The size of the skyrmion decreases progressively until all the skyrmions implode at ~1500 kV/cm. **a,** positive field. **b,** negative field.

Extended Data Fig. 8| Second principle simulation of the evolution of the local polarization texture at the central layer of the $PbTiO_3$ under different external fields. The arrows represent the polarization on the *x*-*y* plane, while the colors represent the component of the out-of-plane polarization as indicated in the legend. The snapshots correspond to Monte Carlo simulations at different electric fields, where the initial configuration for a new magnitude of the field was the relaxed structure from the previous field. **a,** positive field. **b,** negative field.
For the sake of clarity let us assume that the core of the skyrmion has a polarization pointing along the +*z* direction, while it points down along -*z* at the periphery, at null external field. Let us assume also that we switch on an external field parallel to the polarization at the center of the skyrmion, as it is done in panel (a) (positive values of the field). Then, as it is clearly visible from the snapshots at 250 kV/cm and 500 kV/cm, the domain with a polarization parallel to the external field increases at the expenses of the other. The domain wall of the skyrmion has moved, but there will be always a domain wall between the core and the periphery of the skyrmion where the out-of-plane polarization vanishes (see the regions plotted in white delimiting the surface of the skyrmion). There is a tendency of the domain wall to polarize with the appearance of a Bloch component to minimize the energy (see the arrows within the white regions of the panels).[48] This Bloch components of the polarization are perpendicular to the applied field and do not couple with it. Therefore, they will be always present, independently of

the sizes of the domains up and down. These Bloch components closing a loop around the domain wall are precisely at the origin of the non-trivial topological textures (the vortex they form determine why the skyrmion number is +1).

The larger the electric field, the larger the size of the domain that aligns with it (with the criterion chosen for this example, the skyrmion expands). For a critical field, this domain will cover all space and the transition to a monodomain state will be completed. Right before the transition, a singularity appears: the stereographic projection of our dipole patterns does not completely wrap the unit sphere. That is exactly the point where the skyrmion number changes from +1 (non-trivial topological structure) to 0 (trivial case in the monodomain configuration).

Extended Data Fig. 9| Tunable skyrmion size under electric field as a basis for dielectric enhancement $[(SrTiO_3)_{16}/(PbTiO_3)_{16}]_8$ superlattice. a, Experimental line cuts through skyrmion diffuse scattering showing 1st and 2nd order satellites, including their suppression and enhancement, respectively, under external electric field. **b,** Electric field dependency of 1st and 2nd order satellites shown in **a,** determined experimentally. **c,** Phase field model of vertical polarization distribution versus electric field depicting planar cuts (80 nm × 80 nm) through the center and parallel with the $PbTiO_3$ layer. Insets show FFT averages for all $PbTiO_3$ layers of the superlattice, which indicates the emergence of 2nd order diffuse scattering skyrmion ring in addition to the dominant 1st order diffuse scattering skyrmion ring. The 2nd order ring intensity is enhanced under application of electric field relative to without field. **d,** Comparison between the experimentally estimated and phase-field calculated skyrmion areal fraction inside $PbTiO_3$ layers of the superlattice. **g,** Comparison between the experimentally measured (blue) and phase- field calculated (red) dielectric permittivity of the superlattice, which is closely mapped with electric field dependent normalized satellite intensity of skyrmion calculated from reciprocal space (dark gray, right axis).

Extended Data Fig. 10| Temperature control of skyrmion of **$[(SrTiO_3)_{16}/(PbTiO_3)_{16}]_8$ superlattice. a-c,** Temperature dependent three-dimensional, synchrotron-based symmetric reciprocal space mapping about the (002) diffraction condition of the $SrTiO_3$ substrate. The satellite peaks along (100) direction (side-lobes) which correspond to the skyrmions. **d,** The in-

plane satellite peaks intensity (skyrmion peaks) diminishing upon heating and completely disappeared ~600K. **e,** Comparison between the temperature-dependent experimentally measured and phase- field calculated out-of-plane dielectric permittivity of the superlattice.

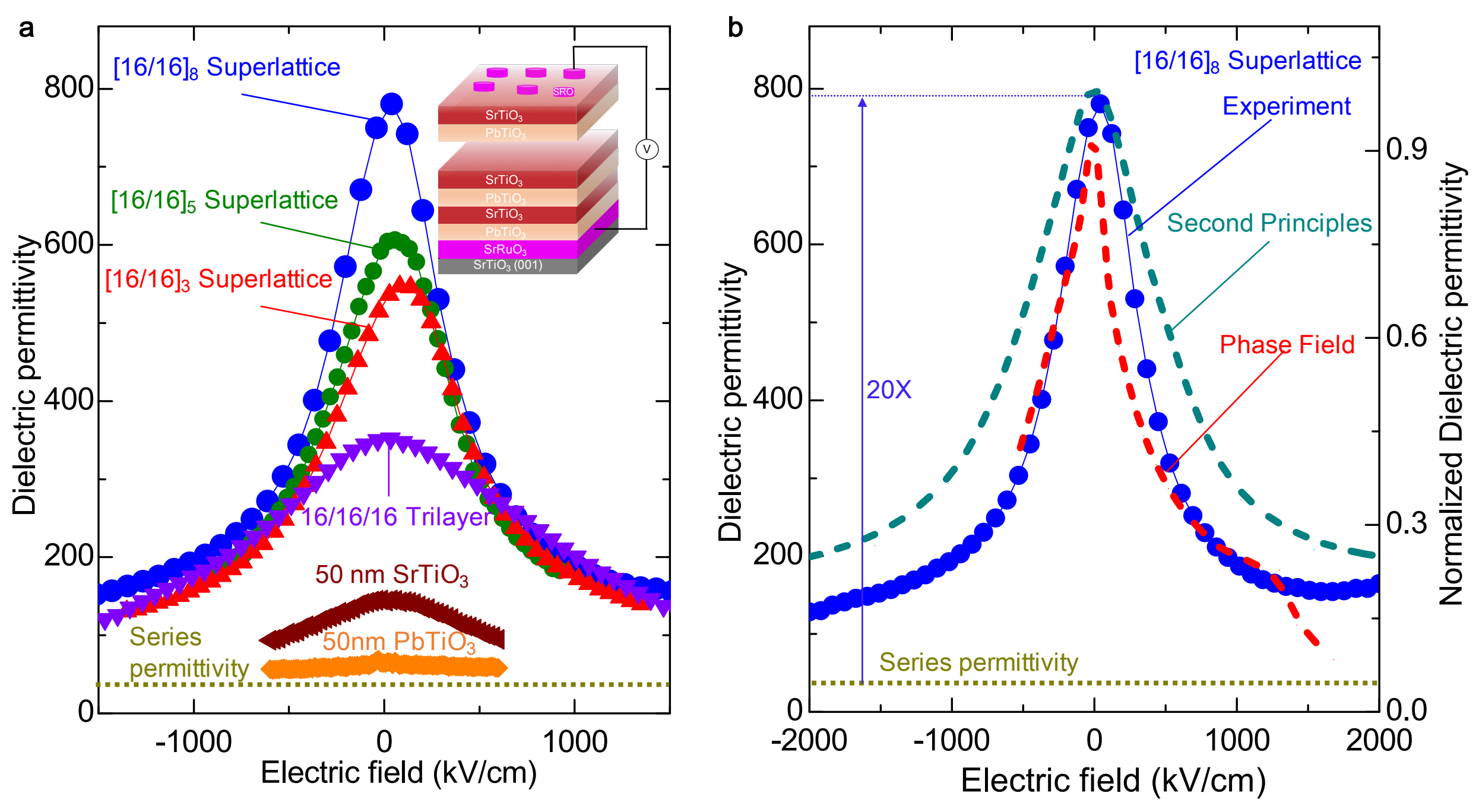
a
[16/16]8 Superlattice
[16/16]5 Superlattice
[16/16]3 Superlattice
16/16/16 Trilayer
50 nm SrTiO3
50nm PbTiO3
Series permittivity
SRO
SrTiO3
PbTiO3
SrRuO3
SrTiO3 (001)
V
Dielectric permittivity
Electric field (kV/cm)
0
200
400
600
800
-1000
0
1000
b
[16/16]8 Superlattice
Experiment
Second Principles
Phase Field
20X
Series permittivity
Dielectric permittivity
Normalized Dielectric permittivity
Electric field (kV/cm)
0
200
400
600
800
0.0
0.3
0.6
0.9
-2000
-1000
0
1000
2000

a

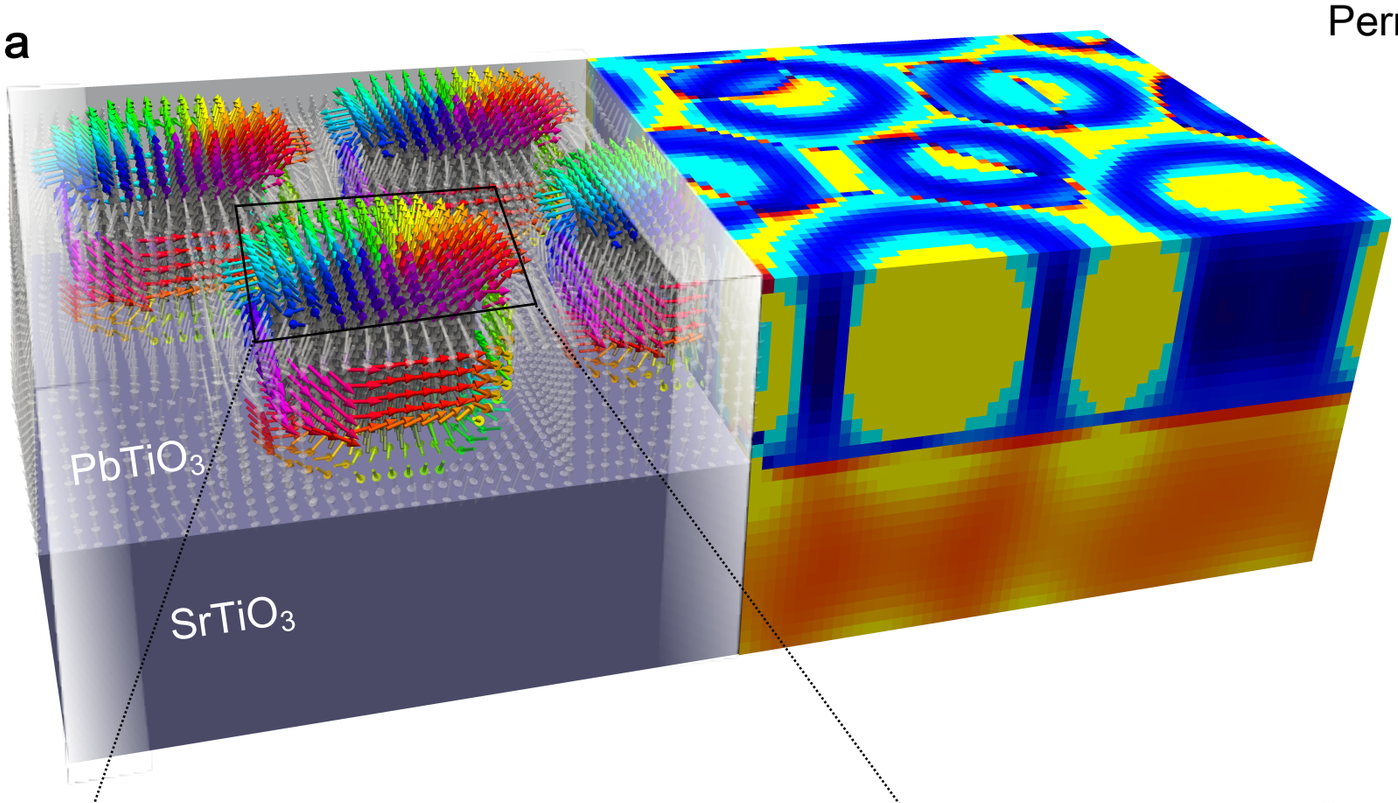
PbTiO3
SrTiO3
Permittivity
4000
2000
0
-2000
-4000

b

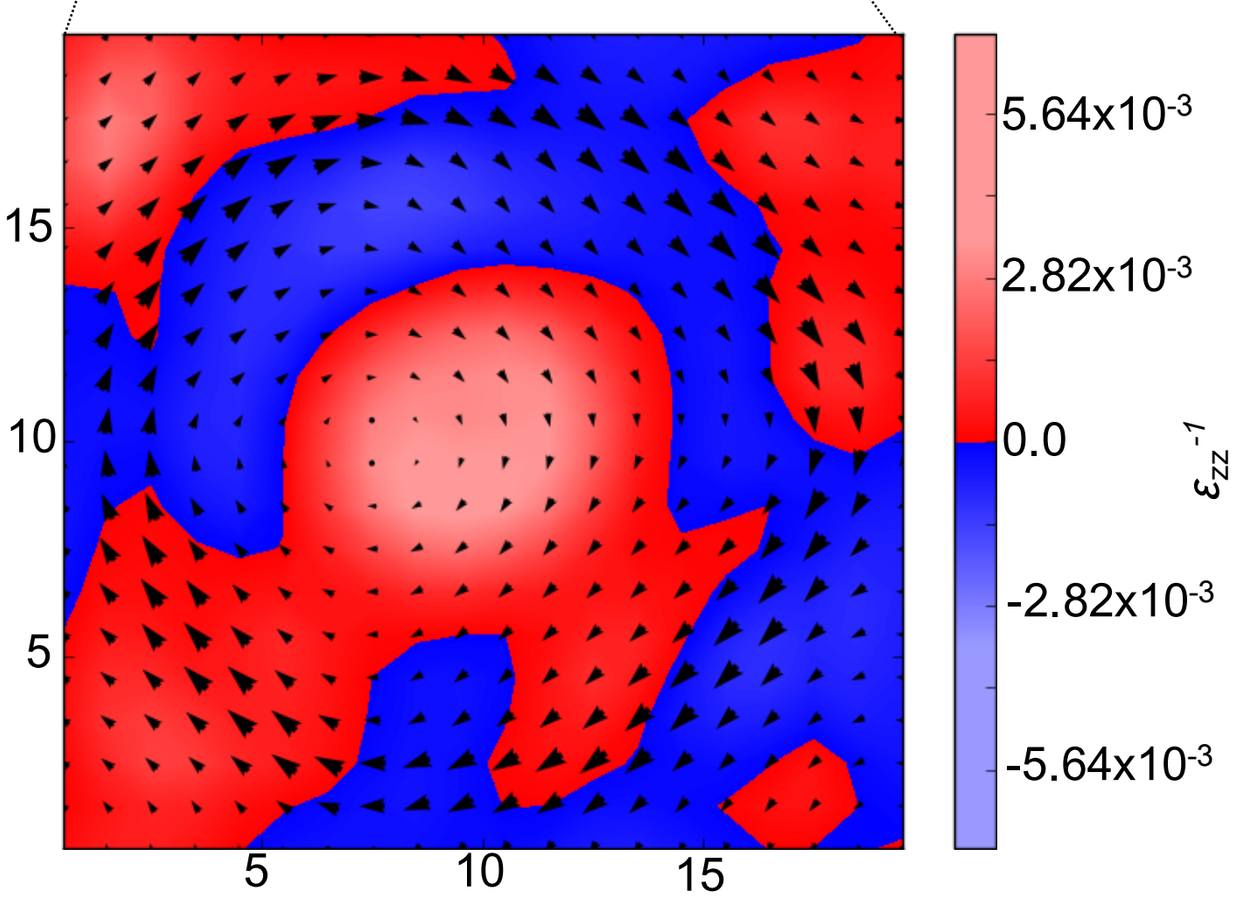
15
10
5
5
10
15
5.64x10-3
2.82x10-3
0.0
-2.82x10-3
-5.64x10-3
εzz-1

c

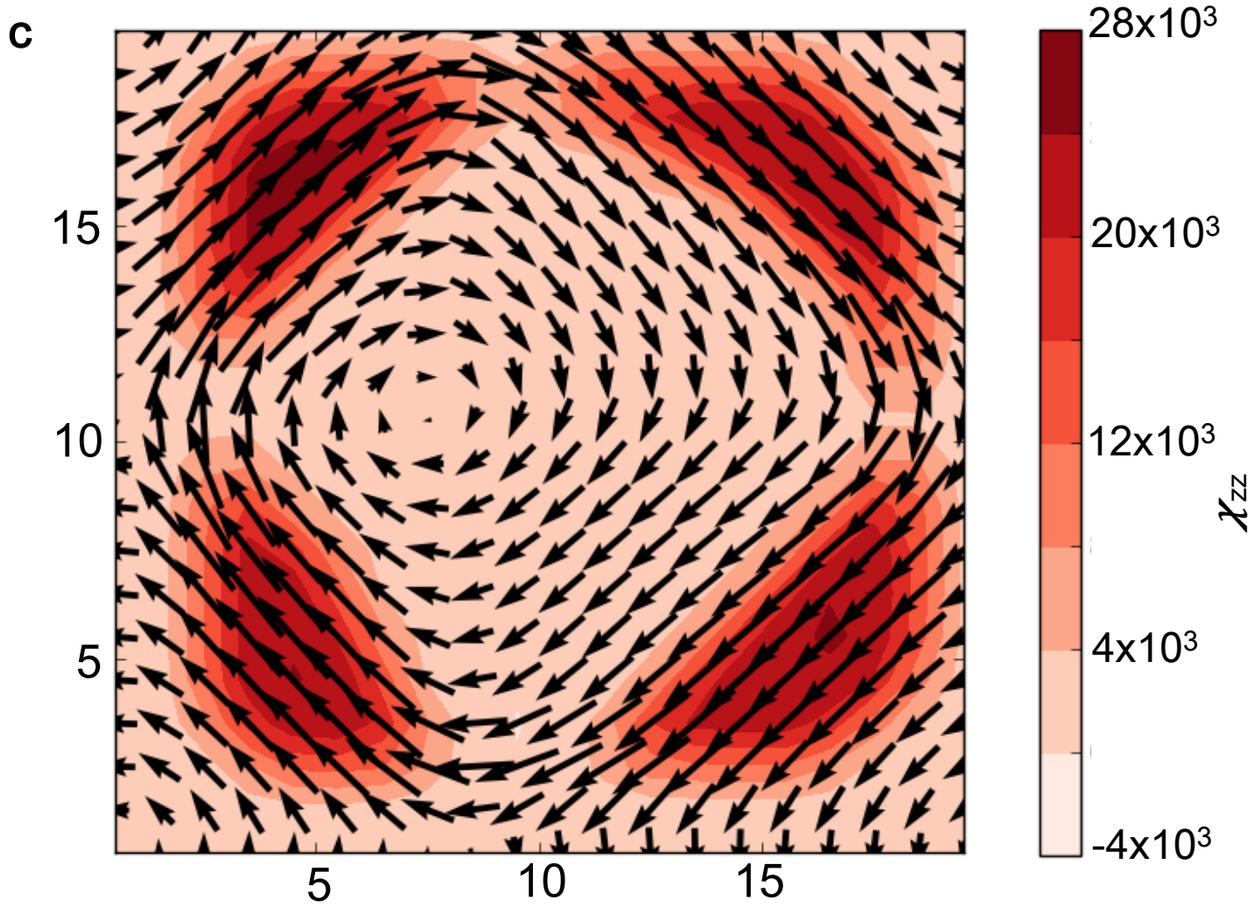
15
10
5
5
10
15
28x10³
20x10³
12x10³
4x10³
-4x10³
χzz

d

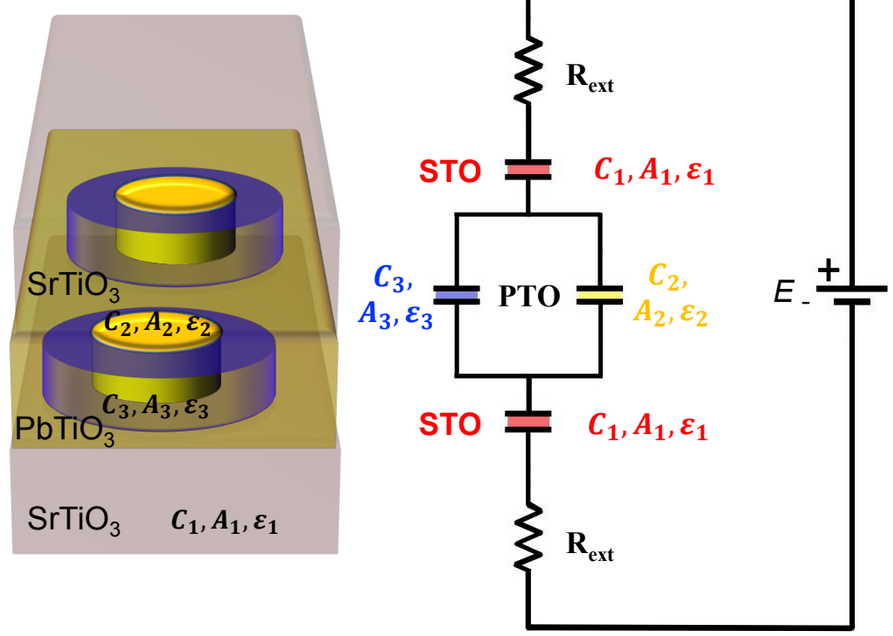
SrTiO3
C2, A2, ε2
C3, A3, ε3
PbTiO3
SrTiO3 C1, A1, ε1
Rext
STO
C1, A1, ε1
C3, A3, ε3
PTO
C2, A2, ε2
STO
C1, A1, ε1
Rext
E

e

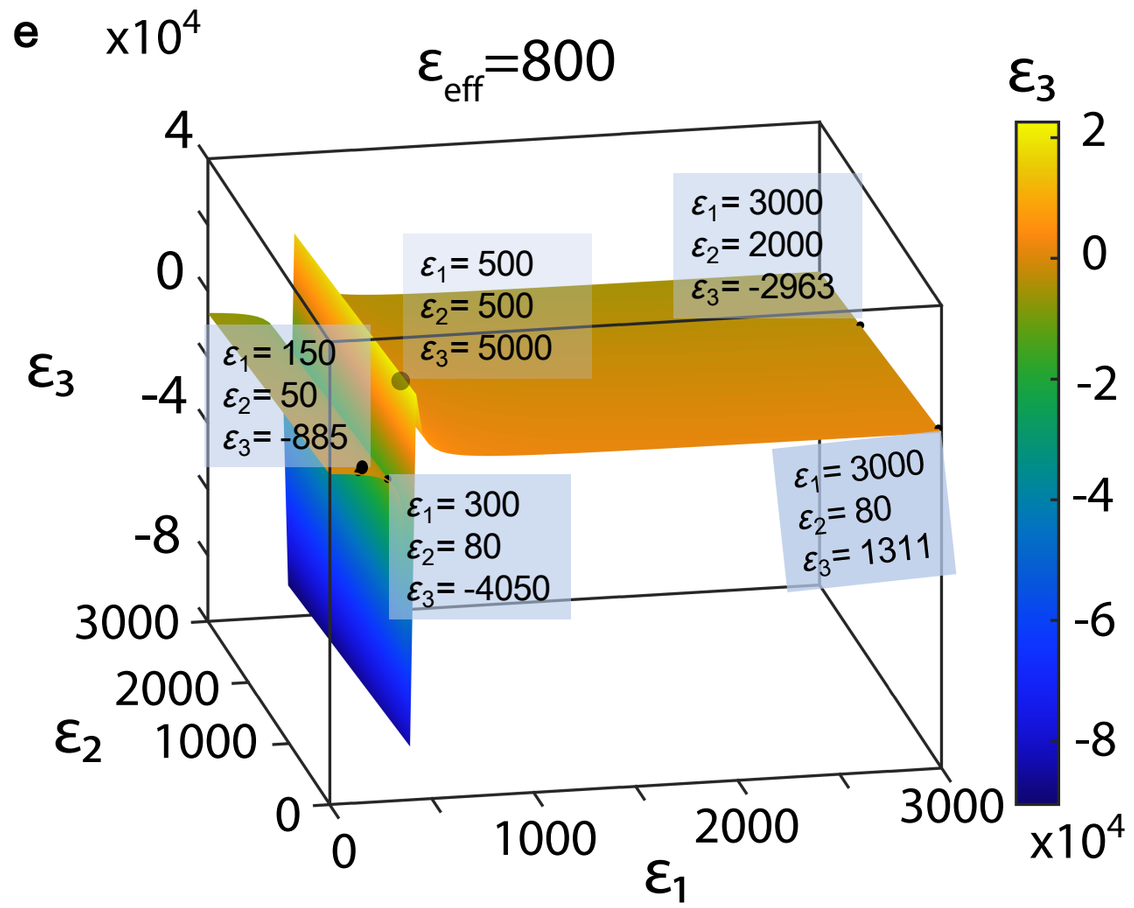
x10⁴
εeff=800
ε3
4
0
-4
-8
ε1= 3000
ε2= 2000
ε3= -2963
ε1= 500
ε2= 500
ε3= 5000
ε1= 150
ε2= 50
ε3= -885
ε1= 300
ε2= 80
ε3= -4050
ε1= 3000
ε2= 80
ε3= 1311
3000
2000
1000
0
ε2
0
1000
2000
3000
ε1
ε3
2
0
-2
-4
-6
-8
x10⁴

f

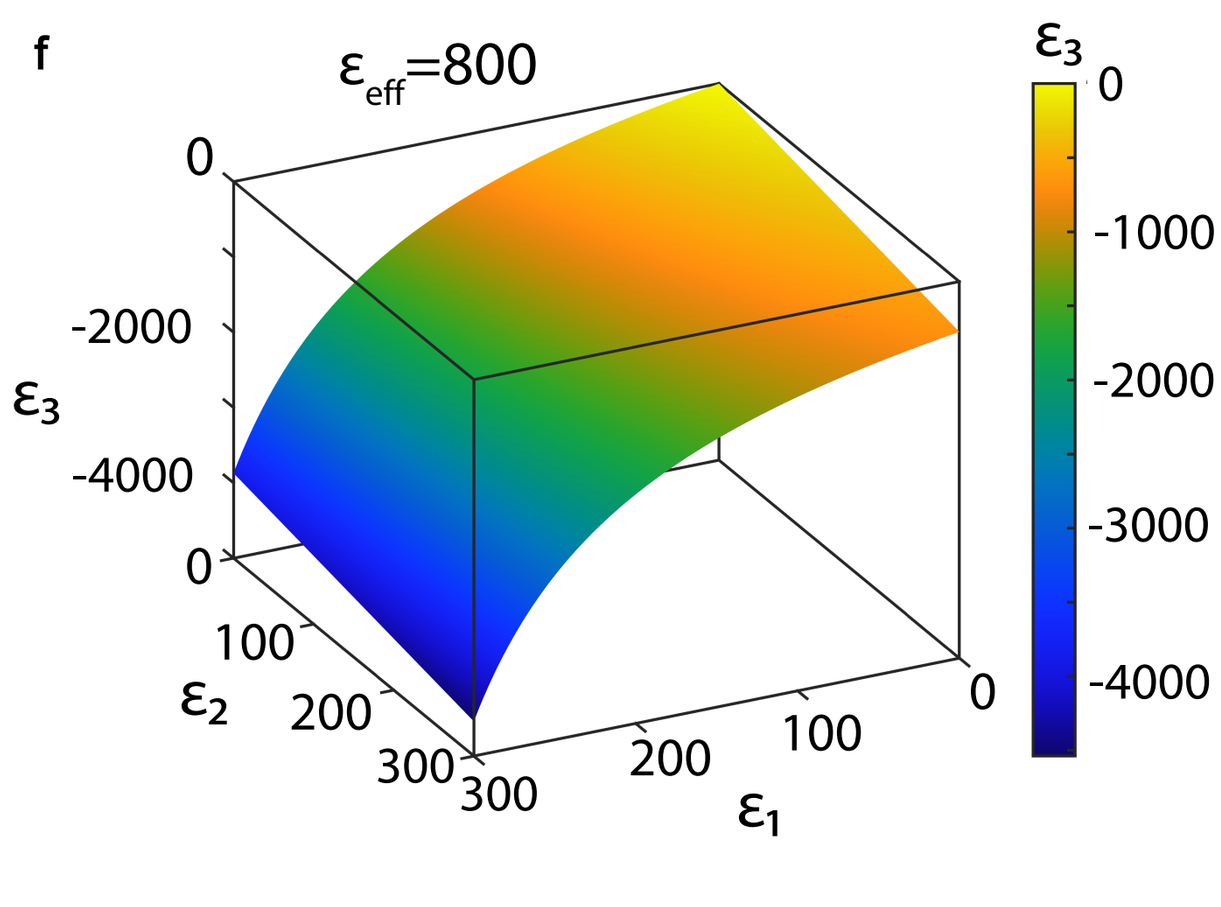
εeff=800
ε3
0
-2000
-4000
0
100
200
300
ε2
0
100
200
300
ε1
ε3
0
-1000
-2000
-3000
-4000

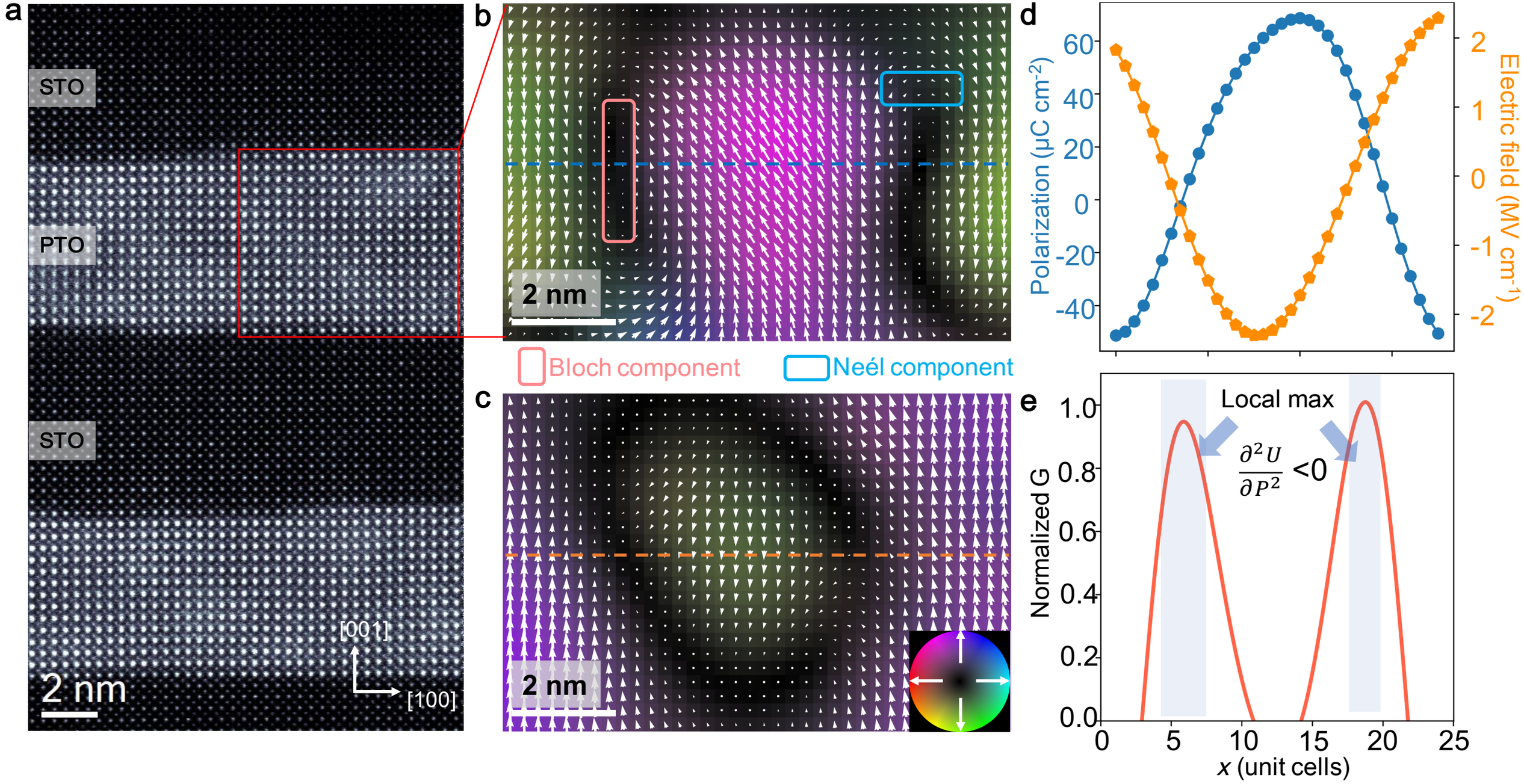
a
STO
PTO
STO
2 nm
[001]
[100]
b
2 nm
Bloch component
Neél component
c
2 nm
d
Polarization (μC cm-2)
Electric field (MV cm-1)
60
40
20
0
-20
-40
2
1
0
-1
-2
e
Local max
$\frac{\partial^2 U}{\partial P^2}$ <0
Normalized G
1.0
0.8
0.6
0.4
0.2
0.0
0
5
10
15
20
25
x (unit cells)

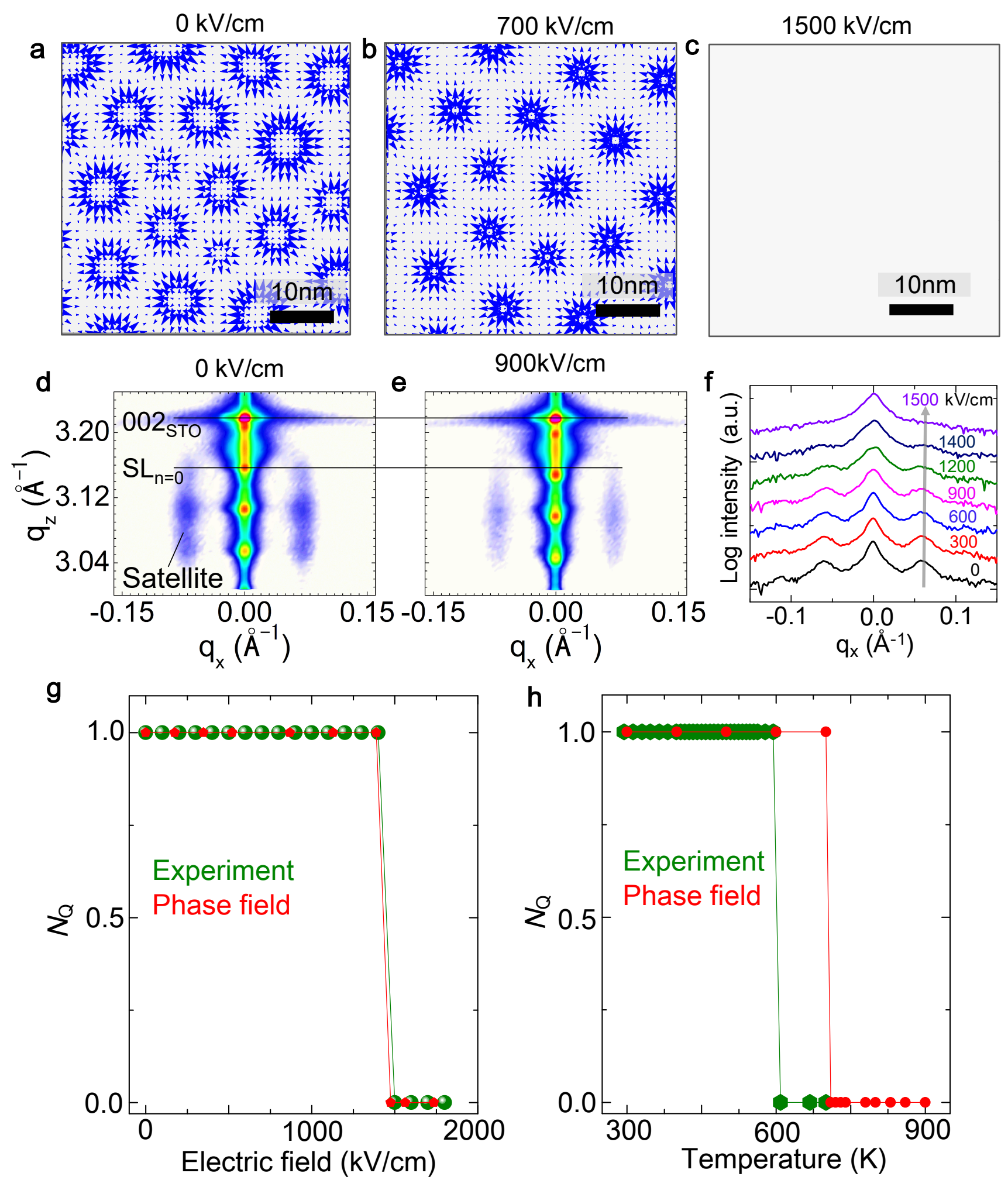
a
0 kV/cm
10nm
b
700 kV/cm
10nm
c
1500 kV/cm
10nm
d
0 kV/cm
002STO
SLn=0
Satellite
3.20
3.12
3.04
qz (Å−1)
-0.15
0.00
0.15
qx (Å−1)
e
900kV/cm
-0.15
0.00
0.15
qx (Å−1)
f
Log intensity (a.u.)
1500 kV/cm
1400
1200
900
600
300
0
-0.1
0.0
0.1
qx (Å-1)
g
1.0
0.5
0.0
NQ
Experiment
Phase field
0
1000
2000
Electric field (kV/cm)
h
1.0
0.5
0.0
NQ
Experiment
Phase field
300
600
900
Temperature (K)

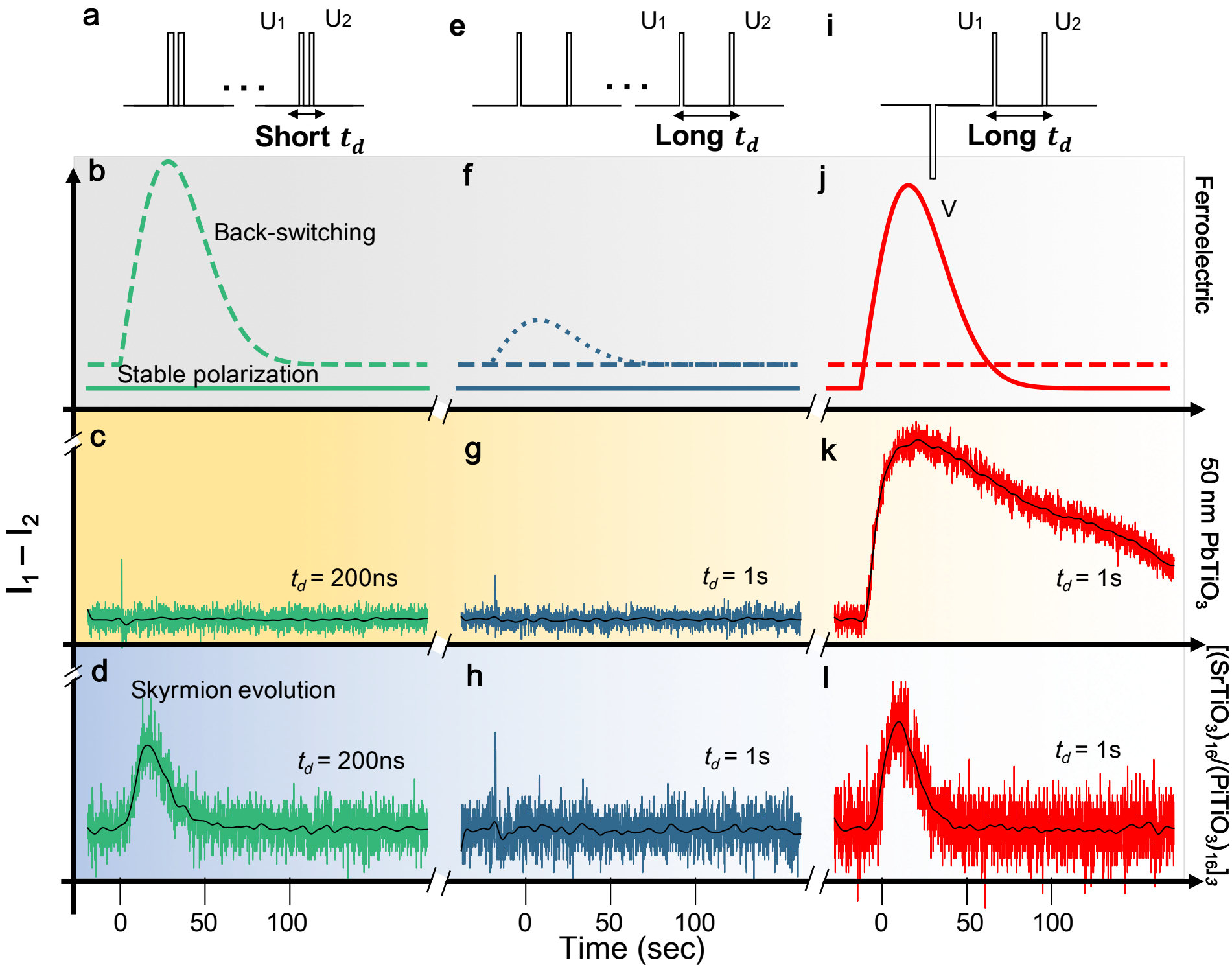
a
U1
U2
Short t_d
e
U1
U2
Long t_d
i
U1
U2
Long t_d
b
Back-switching
Stable polarization
f
j
V
Ferroelectric
c
t_d = 200ns
g
t_d = 1s
k
t_d = 1s
50 nm $PbTiO_3$
d
Skyrmion evolution
t_d = 200ns
h
t_d = 1s
l
t_d = 1s
$[(SrTiO_3)_{16}/(PTiO_3)_{16}]_3$
$I_1 - I_2$
0
50
100
0
50
100
0
50
100
Time (sec)